Available online at www.sciencedirect.com
ScienceDirect
Icarus 186 (2007) 152–177
ICARUS
www.elsevier.com/locate/icarus

Radar observations and a physical model of Asteroid 1580 Betulia

Christopher Magri [a,*], Steven J. Ostro [b], Daniel J. Scheeres [c], Michael C. Nolan [d], Jon D. Giorgini [e], Lance A.M. Benner [b], Jean-Luc Margot [f]

[a] *University of Maine at Farmington, 173 High Street—Preble Hall, Farmington, ME 04938, USA*
[b] *300-233, Jet Propulsion Laboratory, California Institute of Technology, Pasadena, CA 91109-8099, USA*
[c] *Department of Aerospace Engineering, University of Michigan, 1320 Beal Avenue, Ann Arbor, MI 48109-2140, USA*
[d] *Arecibo Observatory, HC3 Box 53995, Arecibo, PR 00612, USA*
[e] *301-150, Jet Propulsion Laboratory, California Institute of Technology, Pasadena, CA 91109-8099, USA*
[f] *Department of Astronomy, Cornell University, Ithaca, NY 14853, USA*

Received 4 June 2006; revised 1 August 2006

Available online 23 October 2006

Abstract

We report Arecibo (2380-MHz, 13-cm) observations of Asteroid 1580 Betulia in May–June 2002. We combine these continuous-wave Doppler spectra and delay-Doppler images with optical lightcurves from the 1976 and 1989 apparitions in order to estimate Betulia's shape and spin vector. We confirm the spin vector solution of Kaasalainen et al. [Kaasalainen, M., and 21 colleagues, 2004. Icarus 167, 178–196], with sidereal period $P = 6.13836$ h and ecliptic pole direction $(\lambda, \beta) = (136°, +22°)$, and obtain a model that resembles the Kaasalainen et al. convex-definite shape reconstruction but is dominated by a prominent concavity in the southern hemisphere. We find that Betulia has a maximum breadth of 6.59 ± 0.66 km and an effective diameter of 5.39 ± 0.54 km. These dimensions are in accord with reanalyzed polarimetric and radar data from the 1970s. Our effective diameter is 15% larger than the best radiometric estimate of Harris et al. [Harris, A.W., Mueller, M., Delbó, M., Bus, S.J., 2005. Icarus 179, 95–108], but this difference is much smaller than the size differences between past models. Considering orbits of test particles around Betulia, we find that this asteroid's unusual shape results in six equilibrium points close to its equatorial plane rather than the usual four points; two of these six points represent stable synchronous orbits while four are unstable. Betulia's close planetary encounters can be predicted for over four thousand years into the future.

Keywords: Asteroids; Radar observations

1. Introduction

Asteroid 1580 Betulia was discovered on May 22, 1950, by E.L. Johnson at the Union Observatory in Johannesburg, South Africa. Betulia is an Earth-crossing Amor asteroid (Shoemaker et al., 1979) and was only the fourteenth near-Earth asteroid (NEA) to be found. Its unusually high orbital inclination of 52°, along with its status as a C-class (carbonaceous) object, led to speculation that it is an extinct comet nucleus (e.g., Drummond and Wisniewski, 1990). But its most unusual feature is its triple-peaked lightcurve. Tedesco et al. (1978) used data from the favorable 1976 opposition to show that at large solar phase angles Betulia exhibits three pairs of brightness extrema per rotation, whereas almost all other asteroids have double-peaked lightcurves and a few (such as 4 Vesta) have single-peaked lightcurves produced by albedo variegation.

Although Tedesco et al. considered the possibility of albedo spots, they were able to explain their data qualitatively by means of shape alone. Their model resembles what one would get by starting with a prolate spheroid (with elongation 1.21) that spins about its shortest (z) axis, and then removing an entire quadrant in the xy plane.

Kaasalainen et al. (2004) took a different approach to estimating Betulia's shape: they inverted lightcurve data from 1976 and 1989 to estimate the spin vector while simultaneously generating a convex-definite shape model, similar to what one would obtain by "gift-wrapping" the actual asteroid. Their

* Corresponding author. Fax: +1 207 778 7365.
E-mail address: magri@maine.edu (C. Magri).

0019-1035/$ – see front matter
doi:10.1016/j.icarus.2006.08.004

spin vector has sidereal period $P = 6.13836$ h and pole direction $(\lambda, \beta) = (136°, +22°)$ with an error radius of 5–10°. Their shape model has axis ratios $a/b = 1.1$ and $b/c = 1.4$, and is "very peculiar with a large planar area on one side." Kaasalainen and Torppa (2001) point out that the locations of concavities in an asteroid are revealed as large planar sections in the best-fit convex-definite model; hence Kaasalainen et al. (2004) note that the flat side of their Betulia model may represent a "considerable" concavity.

A separate issue is the absolute size of Betulia. Tedesco et al. used polarimetric data to derive the visual albedo and hence the mean diameter, obtaining values of 6.3 and 7 km for two possible laws relating polarimetric slope to albedo. Pettengill et al. (1979) used continuous-wave (CW) radar spectra from the 1976 apparition to obtain a zero-crossing Doppler bandwidth of 26.5 ± 1.5 Hz, which could be combined with the known rotation period to show that a lower bound on Betulia's maximum breadth is 5.8 ± 0.4 km. Lebofsky et al. (1978) combined visual photometry, 10.6-μm radiometry, and the standard thermal model to derive a mean diameter of 4.20 ± 0.20 km and geometric visual albedo $p_v = 0.108 \pm 0.012$. Since this diameter conflicts with the polarimetric and radar results, Lebofsky et al. also considered a thermal model that assumes high thermal inertia (i.e., bare bedrock or large rocks rather than fine-grained regolith) and hence significant infrared radiation from the night side; this model yielded a diameter of 7.48 ± 0.34 km and an albedo of 0.034 ± 0.004. This diameter estimate is in accord with the polarimetric and radar values.

More recently, this agreement has been called into question by Harris et al. (2005), who observed Betulia at five thermal infrared wavelengths in 2002. Harris et al. analyzed these data using the NEA thermal model (NEATM), which, unlike the two simple models considered by Lebofsky et al. (1978), treats the infrared "beaming parameter" η as an adjustable parameter, effectively adjusting the temperature distribution across the model's surface so as to be consistent with the asteroid's observed color temperature. This procedure resulted in an effective diameter estimate of 3.8 ± 0.6 km, significantly smaller than values obtained in earlier studies, and a visual albedo of 0.11 ± 0.04. Harris et al. explored this discrepancy by carrying out a second analysis, this time combining a detailed thermophysical model with the Kaasalainen et al. (2004) convex-definite shape model. The resulting effective diameter and visual albedo are 4.57 ± 0.46 km and 0.077 ± 0.015, respectively; this diameter is larger than the NEATM-based estimate but still smaller than earlier estimates. Both the Lebofsky et al. and Harris et al. p_v estimates are plausible for C-class asteroids, so we cannot use this criterion to choose between models.

Betulia's most recent favorable opposition was in 2002, when it approached to within 0.238 AU of Earth, and we took this opportunity to observe it once again with radar, this time obtaining both CW spectra and delay-Doppler images. As discussed by Ostro et al. (2002), radar data can be used to constrain the target's orbit, size, shape, and spin vector, its near-surface roughness at decimeter scales (due to surface rocks, buried rocks, and subsurface voids), and its near-surface bulk density, which can tell us about mineralogy (e.g., metal content—see Ostro et al., 1991a) or about near-surface porosity (Magri et al., 2001). Most importantly for Betulia, concavities leave a strong signature in delay-Doppler images. The primary goals of our radar experiment were to reconstruct Betulia's shape—including any possible concavities—and to determine its absolute size.

The next section describes our observations. Section 3 discusses in some detail how we use our modeling software to reconstruct the shape of a radar target. Section 4 presents the resulting shape model, and Section 5 considers the implications of our improved radar astrometry. Section 6 characterizes Betulia's gravitational environment, discussing the possible orbits in its vicinity. Finally Section 7 summarizes our results. Appendix A contains detailed information on the delay-Doppler impulse response function and on delay-Doppler image calibration, Appendix B fully describes the penalty functions used by our modeling software, and Appendix C lists Betulia's gravity coefficients.

2. Observations and data reduction

2.1. Delay-Doppler images

2.1.1. Observing scheme

The delay-Doppler images discussed here were obtained in May–June 2002 (see Table 1) at the Arecibo Observatory. For each observation (or "run") we transmitted a circularly polarized monochromatic signal at about 2380 MHz. In order to compensate for the Doppler shift due to relative motion between the telescope and the target's center of mass (COM), we generated ephemeris predictions of the COM Doppler shift, and continuously adjusted the transmission frequency so that hypothetical echoes from the COM would return at 2380.000005 MHz if our ephemeris were exactly correct. (The extra 5 Hz "transmit offset" serves to make the direction of positive Doppler clear in case of error in the instrumental setup or in the data analysis.) We used the early observations in the experiment to refine the orbit and then generated a new prediction ephemeris, so that we avoided delay and Doppler smearing produced by uncompensated changes in the COM delay and Doppler shift over a run's duration.

The transmitted signal was phase-modulated via a pseudorandom binary code, each element (bit) of which is an instruction either to invert or not to invert the transmitted sinusoid for a duration of b (for "baud length") seconds. After L elements the code repeats itself; thus the code repetition time is $p = Lb$. Such repeating "maximum-length codes" are designed to have a very low value for the autocorrelation function ($= -1/L$) for any lag other than zero, a property that was important when we decoded the echoes to produce images (see below).

We transmitted this modulated signal for a duration almost equal to the round-trip time (RTT) to the target, then switched to receive mode for an equal duration, measuring the echo signal in both the same circular polarization as was transmitted (SC) and the opposite circular polarization (OC). Echoes in each polarization were received as analog voltage signals, amplified, mixed down to baseband, and convolved with a rectangular fil-

Table 1
Observations

2002 observing date (UT)	Type	Runs	Receive start–end (UT)	RA (°)	Dec. (°)	Dist. (AU)	δ (°)	Rot. phase (°)	Orbital solution	Code	Baud (μs)	spb	Δf (Hz)	Power (kW)
May 28–29	Ranging	1	23:53:49–23:57:39	197	+23	0.238	−44	120–123	32	8191	4.0	1	0.954	560
	Ranging	1	00:02:47–00:06:37	197	+23	0.238	−44	128–132	32	8191	4.5	1	0.848	560
	CW	5	00:13:00–00:48:38	197	+22	0.238	−44	137–171	32	–	–	–	1.000	547
	Delay-Doppler	10	00:53:56–02:10:10	197	+22	0.238	−44	179–253	32	8191	0.5	1	0.954	548
	Delay-Doppler	2	02:15:50–02:27:36	197	+22	0.238	−44	259–271	32	4095	1.0	2	0.954	545
May 29–30	CW	1	23:41:35–23:45:25	196	+19	0.238	−43	79–83	34	–	–	–	1.000	834
	Delay-Doppler	11	23:53:33–01:28:15	196	+19	0.238	−43	91–183	34	2047	2.0	2	0.954	839
	Delay-Doppler	6	01:32:21–02:19:30	196	+19	0.238	−43	191–231	34	2047	2.0	2	0.954	450
May 31–Jun. 1	CW	1	23:47:10–23:51:00	193	+11	0.241	−41	30–33	34	–	–	–	1.000	825
	Delay-Doppler	15	23:58:39–01:55:01	193	+11	0.241	−41	41–155	34	2047	2.0	2	0.954	817
Jun. 1–2	CW	1	23:30:29–23:32:39	192	+7	0.245	−39	346–348	34	–	–	–	1.000	823
Jun. 2–3	Delay-Doppler	9	23:34:10–00:44:34	191	+4	0.249	−38	321–30	34	2047	2.0	2	0.954	605

Notes. All experiments involved transmission at 2380 MHz and reception in both OC and SC polarizations. On each line we give the observing date; the type of observation; the number of transmit–receive cycles, or runs; the starting and ending receive times; right ascension, declination, and distance from Earth; subradar latitude δ at mid-receive; the range of rotation phase covered (with zero phase occurring at UT 2002 Jun. 03 00:11:53); the orbital solution used for our delay-Doppler ephemeris predictions; the length of the repeating binary phase code; the baud length and the number of samples per baud; the raw frequency resolution Δf of our reduced data; and the transmitted power. Plane-of-sky motion was taken into account when computing rotation phase.

ter matched to the baud length. We then took digital samples of the complex voltage every w seconds. Typically b is an integer multiple of w; denoting this integer as s, we refer to this procedure as taking s samples per baud. (The advantage of using $s > 1$ is discussed at the end of Appendix A.) Finally we wrote these samples to disk for later processing.

2.1.2. Data reduction

The echoes had to be decoded in delay, since each data sample represents contributions from multiple delay lags: power that was transmitted earlier and then scattered off relatively distant parts of the target as well as power that was transmitted later and then scattered from relatively nearby parts of the target. We accomplished this by cross-correlating our time series of voltages with a copy of the binary phase code. In other words, we decoded a particular delay lag by multiplying the received time series by a suitably lagged copy of the code and then taking the mean value of this product. The fact that the code's autocorrelation function is nearly zero for nonzero lag ensured that the contributions from the "wrong" lags summed to nearly zero.

[Since the code is periodic, we actually carried out the cross-correlation in the frequency domain in order to speed up the computation. First we created a copy of the code in which each code element is repeated s consecutive times, and then we computed C^*, the complex conjugate of the fast Fourier transform (FFT) of this copy. Next we obtained D, the FFT of the data; this had to be done in pieces, since there were too many samples per run to transform all of them at once. For each piece we first subtracted the mean complex voltage from the data in order to minimize any constant offsets from the digitization, then performed an FFT to obtain D. These FFT computations were sped up by means of the overlap-save sectioning method (e.g., Brigham, 1988). Finally we took the product C^*D and performed an inverse FFT to go back to the time domain.]

The maximum number of lags that can be decoded is Ls, the number of voltage samples per code repetition time. We typically decode all possible lags, but it is possible to decode only a subset within each baud length—say, every other lag for $s = 4$. We denote the number of decoded lags (image rows) per baud as χ.

Thus we obtained a decoded voltage time series for each of N image rows, where $N = L\chi$. The delay resolution is $\Delta d = b/\chi$, so the unaliased delay range covered is $N\Delta d = Lb = p$. For each row we now performed an n-point FFT to get a Doppler spectrum whose width is the unaliased bandwidth $B = 1/p$ and whose frequency resolution is $\Delta f = B/n = 1/(np)$, and then took the complex square to obtain power. Any power at frequencies outside the range $[-B/2, B/2]$ is aliased to a different Doppler frequency (image column) within that range. This procedure was carried out for blocks of nN decoded samples at a time (covering np of observing time), each block yielding an $n \times N$ image that represented one "look," a single estimate of the echo's delay-Doppler power distribution.

This delay-Doppler image is quite different from an optical image of the target, and not merely in the observing wavelength. Both dimensions of an optical image are angular dimensions that are directly proportional to spatial dimensions. For a radar image, the delay dimension is directly proportional to a spatial dimension (distance from Earth) but the Doppler dimension is directly proportional to radial *velocity*, which depends not only on the spatial position of a given scattering element but also on the target's spin vector. Furthermore, at a given moment two or more noncontiguous scattering elements on the target's surface can share the same delay and Doppler values: the mapping from the plane of the sky to a delay-Doppler image is generally a many-to-one mapping (see Fig. 1 of Ostro et al., 2002).

If τ is the integration time (∼RTT) for the run then the number of looks is $N_{\text{looks}} = \tau/(np) = \tau\Delta f$. We incoherently summed these independent estimates, thus reducing the fractional noise fluctuation by a factor of $\sqrt{N_{\text{looks}}}$. Finally we computed the mean noise power and r.m.s. noise fluctuation within a signal-free subset of the image, subtracted the mean from the image, and divided the result by the r.m.s. fluctuation, thus obtaining a normalized image with zero mean and unit r.m.s. noise fluctuation.

Since the code is periodic, any signal that is earlier than the first delay lag or later than the last one is "wrapped around" (aliased) to a different lag. In order to avoid delay aliasing, the target's delay depth must be less than the unaliased delay range p; in order to avoid Doppler aliasing, the target's bandwidth (due to rotation) must be less than the unaliased bandwidth $B = 1/p$. There is no way to satisfy both of these requirements simultaneously unless the product of the target's delay depth and bandwidth is less than unity: the "spreading criterion" (Green, 1968, p. 34). This criterion is easily satisfied for NEAs such as Betulia; overspreading can be a problem for larger main-belt asteroids and (especially) for planets. Different observing schemes must be employed for overspread targets, such as the "coded long pulse" (or "long code") technique (Sulzer, 1986, 1989; see also Harmon, 2002) in which a nonrepeating binary phase code and a modified reduction algorithm are used in order to spread the delay-aliased signal at each lag across the full unaliased Doppler bandwidth.

2.1.3. Initial observations

Even an NEA, however, has the problem that until its orbit has been precisely constrained, the delay might be off by some integer multiple of the unaliased delay depth p without our knowing it. For example, a signal that appears to be at exactly the predicted delay might in fact be an integer multiple of p earlier or later. We dealt with this delay aliasing problem at the start of the experiment by taking two low-resolution "ranging" images using the same code length but slightly different baud lengths, 4.0 and 4.5 μs. For example, a target that is exactly two codes further away ($2p$ later in delay) than predicted at 4.0 μs will be only 1.78 codes further away than predicted at 4.5 μs, so the latter signal will appear to have shifted *closer* to us by 22% of the image depth ($0.22p$). We used this information to update our ephemeris before performing high-resolution observations.

Our high-resolution runs on the first observing date, with baud lengths of 0.5 and 1 μs, turned out to be too weak to be very useful, so for the remainder of the experiment we used

a 2-μs baud (with $s = 2$) and a 2047-length code; it is these 41 images (reduced with $\chi = 2$) which we have used to model Betulia's shape.

2.2. Doppler spectra

We also obtained eight continuous-wave (CW) Doppler spectra on four dates (see Table 1). The observing procedure was somewhat similar to that used for imaging, except that there was no phase modulation (and hence no delay information and no decoding to perform), the transmit offset was 200 Hz (to move the signal well away from the strong spike at 0 Hz caused by constant offsets in the system), the COM Doppler shift was compensated for by continuously adjusting the receive frequency rather than the transmit frequency, and the sampling rate was 5000 Hz (yielding $B = 5000$ Hz). A linear baseline was subtracted from each power spectrum during the process of normalizing it to zero mean and unit r.m.s. noise fluctuation.

3. Shape modeling

We combined 41 delay-Doppler images and eight CW spectra with 25 lightcurves taken from the Asteroid Photometric Catalogue (Lagerkvist et al., 2001) in order to model Betulia's shape, size, spin state, and radar reflectivity. Our modeling procedure is the same one used in all recently published radar-based asteroid shape reconstructions, so we describe it here in some detail.

3.1. Ellipsoid model

3.1.1. Model parameters

In reconstructing Betulia's shape we started with a triaxial ellipsoid model whose long, intermediate, and short axis lengths are $2a$, $2b$, and $2c$, respectively. We assumed principal-axis rotation, with the spin vector parallel to the short axis. We initialized the rotation period, pole longitude, and pole latitude to the Kaasalainen et al. (2004) values; for some modeling runs we held all three of these parameters fixed, while for others we treated one or more of them as free parameters. Since our observing ephemeris was not perfect, we fit the correction in delay as a second-order polynomial in time. This polynomial also provided us with the (linear) Doppler correction polynomial as a function of time, since Doppler is proportional to the negative of the time derivative of delay.

We assumed a two-parameter radar scattering law, $d\sigma/dA = \rho \cos^n \theta$, where σ is radar cross section, A is physical surface area, and θ is the angle of incidence. In fitting lightcurves, we assumed the optical hybrid scattering law used by Kaasalainen et al. (2001), a weighted sum of Lommel-Seeliger and Lambert contributions. In our ellipsoid modeling, the free parameters were the three axis lengths, the rotation phase at an arbitrary reference epoch, the radar reflectivity ρ, the weighting factor in the optical scattering law (which controls the degree of limb darkening), the three delay correction polynomial coefficients, and (for some modeling runs) the rotation period, pole longitude, and pole latitude. The radar scattering law exponent n was held fixed during each modeling run, although we varied it in a multirun grid search in order to place constraints on its value. We were not interested in modeling Betulia's absolute optical brightness, so we treated all lightcurve data as relative photometry; Kaasalainen and Torppa (2001) claim that this can be a good idea even when absolute photometry is available, as it leads to a cleaner split between the shape/spin solution and the optical scattering law solution.

3.1.2. Modeling algorithm

Our constrained-least-squares shape-modeling program, SHAPE, cycled through the 9–12 free parameters, searching at each step for the best-fit value of one of these parameters while holding all of the others constant (Hudson, 1993). By "best-fit" we mean that the objective function, the sum of reduced chi-square and one or more penalty functions, is at a local minimum. The only penalty function used at the ellipsoid stage of the fit was the "nonpa_uni" penalty, designed to discourage nonprincipal-axis (NPA) models by returning large values when the third axis length $2c$ was not the shortest axis length. (The various penalty functions used by SHAPE are fully described in Appendix B.) The penalty function was multiplied by a user-chosen weighting factor; larger penalty weights meant that the corresponding model property (here NPA rotation) was more strongly discouraged. In this way penalty functions ensured that our model would not possess unusual or implausible physical properties unless the data truly required such properties; since principal-axis rotation is simpler than NPA rotation, our conservative approach was to apply Occam's razor by trying to find a viable principal-axis model before resorting to NPA models.

For each free parameter in the cycle, SHAPE computed the objective function for the unchanged parameter value, then added a user-specified increment *step* to the parameter and computed the new objective function. Based on what it found in comparing the two function values, the program then applied ever-larger steps in the "downhill" direction until finally the objective function started to rise again, at which point we knew that we had reached a local minimum; that is, we "bracketed" the minimum (Press et al., 1992, Section 10.1). Next SHAPE homed in on that minimum; if *more* than one local minimum was present within the bracketed parameter interval, there was no guarantee that we would find the best one. Here we used a modified version of Brent's algorithm (Press et al., 1992, Section 10.2) that allowed us to specify both an absolute tolerance *abstol* and a fractional tolerance *fractol*. The best-fit parameter value x which we finally obtained was within $\pm(fractol|x| + abstol)$ of the parameter value $x_{\min}$ that would truly have minimized the objective function. Different increments, fractional tolerances, and absolute tolerances were used for different parameters; for example, we generally used nonzero *abstol* for angles (e.g., rotation phase at the reference epoch) and nonzero *fractol* for other parameters.

If *step* was too small, the algorithm could get stuck in shallow local minima without ever "noticing" better minima that are not too far away in parameter space; if it were too large, we could step too far and jump from a good local minimum to a

shallower one some distance away. Small *fractol* and *abstol* values were good but resulted in slower fits. Experimentation and subjective judgment were needed to arrive at sensible values.

Each time SHAPE evaluated the objective function for a trial value of the parameter being adjusted at the moment, it "realized" the current ellipsoid model as a 2586-vertex polyhedral solid (with triangular facets) that approximated the ellipsoid. Next, for each CW spectrum, delay-Doppler image, and lightcurve point to be modeled, the model's angular orientation (i.e., rotation phase), position and motion in the plane of the sky, delay correction, and Doppler correction were determined for that observation epoch. For each epoch, the program created a model plane-of-sky (POS) frame—a simulated diffraction-free *optical* image of the model as viewed from Earth at that epoch—that was 9 km on a side with 101 pixels per side. We stress that this simulated POS image inhabited a completely different two-dimensional space (north–south, east–west) than a radar image (delay, Doppler) and was merely an intermediate step along the way to generating simulated radar images and spectra and simulated lightcurve data. SHAPE checked each pixel in the POS frame to determine which triangular model facet was projected onto its center as viewed from Earth, and assigned relevant quantities to the pixel based on that determination: distance, scattering angle, and (for lightcurve points) incidence angle and shadowing status. A Doppler value was assigned based on the pixel's perpendicular distance in the plane of the sky from the projected rotation axis.

(SHAPE assigned incidence and scattering angles to each POS pixel in a way that effectively smoothed the polyhedral model. First, for each vertex in the model it computed a unit "vertex normal" by summing the unit normals to each facet that had that vertex as one of its corners, then normalizing the sum to unit length. Next, for each POS pixel, SHAPE determined which model facet was projected onto the POS pixel center and constructed a linear combination of the vertex normals for the three vertices of that facet, with more weight in this combination given to a vertex that projected closer to the POS pixel center. The program then computed the incidence and scattering angles relative to the direction of that linear combination.)

The program now used all of these quantities to compute each POS pixel's contribution to the simulated data at that epoch. Obtaining the magnitude for each simulated lightcurve point simply involved taking the logarithm of the sum of the POS pixel values. For CW spectra and (especially) delay-Doppler images, the mapping from the plane of the sky to the simulated data is more complicated, and is described in Appendix A.

Finally SHAPE compared the simulated data to the actual data to obtain chi-square. For lightcurve points, chi-square was computed in magnitude space rather than in intensity space. (As a result, the quantity that we call "chi-square" is not literally chi-square distributed.) We chose to treat lightcurve data as relative photometry: before computing chi-square for a given lightcurve, the program shifted the simulated magnitudes so that their variance-weighted mean was equal to the variance-weighted mean of the actual magnitudes. Such a shift minimizes chi-square. For a few modeling runs we also treated radar data as relative photometry, in which case the program minimized chi-square by applying the appropriate multiplicative constant to the cross section values in each simulated image or spectrum. For each image, SHAPE computed this constant by first normalizing each pixel to unit variance and then dividing the sum over pixels of (simulated pixel) (actual pixel) by the sum over pixels of (simulated pixel)^2; an analogous expression was used for each spectrum. This approach prevents us from estimating radar reflectivity ρ, so for our final model we treated radar data as absolute photometry—that is, we did *not* allow the program to improve chi-square by rescaling the simulated images and spectra.

Each delay-Doppler image, CW spectrum, and lightcurve had its own user-specified weighting factor that multiplied its contribution to chi-square (and its degrees of freedom); these weights could be adjusted at the start of a modeling run so as to force the program to pay more attention to certain data than to others. Once chi-square was computed and was divided by the total number of degrees of freedom to obtain reduced chi-square, the values of the various penalty functions (multiplied by the various penalty weights) were added to yield the objective function.

3.2. Harmonic model

Once we obtained the best-fit ellipsoid, we converted it to a model whose surface displacement was described by a spherical harmonic series with a maximum degree of 8. Just as with the ellipsoid fit, the harmonic model was realized as a polyhedral solid before model predictions were generated, although to save computing time we used only 1148 vertices rather than 2586. One difference with respect to the ellipsoid model was that the spherical harmonic series had $(8 + 1)^2 = 81$ coefficients to be fit rather than just three axis lengths. The other difference is that we used three additional penalty functions. One, "inertiadev_uni," kept the model's principal axes close to the body-fixed Cartesian axes (which were simply the ellipsoid's symmetry axes); another, "comdev," kept the center of mass close to the origin (which was the center of the ellipsoid), thus discouraging nonuniform density. The third, "concavity," yielded large values for nonconvex models; we applied this penalty with an especially high weight in order to discourage concavities very strongly.

Kaasalainen and Torppa (2001) and Kaasalainen et al. (2001) have shown that so long as lightcurve data provide adequate orientational coverage, and so long as any albedo markings are not very extensive (e.g., a single albedo spot) and not very bright, convex-definite models based on optical photometry are robust and unique: the fit reliably converges to the 3-D convex hull of the asteroid's actual shape. (Strictly speaking it converges to the "photometric convex hull," a version of the convex hull that has been "trimmed" such that its shadowing properties best mimic those of the actual nonconvex body.) By using a high concavity penalty weight at this stage of the fit we hoped to obtain some of this stability for our quasi-convex-definite harmonic model and to compare the result to the Betulia model presented by Kaasalainen et al. (2004). The

correspondence between the two methods is rough rather than precise: our software fits the target's surface displacement as a sum of spherical harmonic terms, whereas Kaasalainen and Torppa (2001) fit the target's Gaussian curvature as exp(a sum of spherical harmonic terms).

3.3. Vertex model

Finally we took the best-fit harmonic model and converted it to a polyhedral model with 1148 vertices and 2292 triangular facets ($= 2 \times 1148 - 4$), thus entering the "vertex" stage of the fit. Each vertex was assigned a base displacement that lay on the surface of the best-fit ellipsoid to the harmonic model, and as the fit proceeded the vertex was allowed to move along the direction normal to that ellipsoid. SHAPE sought the vertex deviation from the base displacement (positive to move the vertex outward, negative to move it inward) that minimized the objective function. Since the model's shape was now determined by the values of not 3 or 81 but 1148 free parameters, this final stage of the fit took up the bulk of the computing time. We employed one additional penalty function at this stage, "nonsmooth," to discourage small-scale topographical roughness (whether concave or convex). We also lowered the concavity penalty weight so that the software could add any necessary concavities to fit the data; as will be described later, Betulia has a prominent concavity that is so obvious in our delay-Doppler images that even the high concavity penalty weight used during the harmonic fit could not entirely suppress it.

3.4. General modeling considerations

The modeling procedure outlined above required much subjective input. We had to choose the initial values of the free parameters in our ellipsoid model; since the evolution of our model (i.e., its path through n-dimensional parameter space) depended on our starting point, we tried numerous runs with different starting points, and also considered the effects of different *step* increments. The penalty weights, and any changes in these weights as the fit proceeded, needed to be chosen based on trial and error. For example, if we subjectively determined that a finished model was too spiky to be realistic, we raised the nonsmooth penalty weight for the next modeling run; or if we visually compared our delay-Doppler images with the simulated images and decided that some feature appearing on a particular observing date was important and was not being fit closely enough, we tried other starting points or perhaps lowered some penalty weight(s). The maximum harmonic degree for the harmonic fit, and the number of vertices in the final polyhedral model, had to be chosen as a tradeoff between model detail and computer run time. (Naturally we also had to consider how much detail could be realistically constrained by our data.) Finally, we had the freedom to set the relative weights of the various images, spectra, and lightcurves for the purpose of calculating chi-square. One method of dealing with a hard-to-fit delay-Doppler feature was to increase the weights of the images in which it appears—perhaps by a factor of 2 or even 200. At the very least, we needed to choose the relative weights of images vs spectra vs lightcurves. We tried to give lightcurves enough weight that they would influence the model (i.e., prevent it from going astray), but not so much that they would dominate the radar data; we wanted spectra to be influential enough to constrain Betulia's instantaneous zero-crossing bandwidth (and hence its maximum breadth and its elongation). In all we tried to err on the side of investigating too many possibilities rather than too few, so that we can be confident in the model we have finally adopted.

4. Modeling results

Fig. 1 shows 41 delay-Doppler images alongside the corresponding "fit" images synthesized from our model and the plane-of-sky views of the model. (The plane-of-sky views are the simulated optical "POS frames" discussed in Section 3.1.2.) The eight CW spectra and superimposed fit spectra are shown in Fig. 2. Only OC images and spectra are displayed in these two figures, since only this polarization sense was used for modeling. The 25 lightcurves and superimposed fits are displayed in Fig. 3. The model's properties are summarized in Table 2. The upper panel of Fig. 4 shows six smoothed renderings of the model as viewed along its three principal axes; regions of the surface that were never viewed by the radar, or that were only viewed at scattering angles greater than 60° (thereby producing relatively weak echoes), are shaded yellow. The lower panel of Fig. 4 shows the model as viewed from the same six directions, but these renderings are unsmoothed and are color-coded for gravitational slope (the angle that a plumb line would make with the local normal to the surface) under the assumption of uniform density and taking into consideration the asteroid's rotation.

4.1. Shape

In the preceding section we described an intermediate "harmonic" stage of the modeling process in which we used a spherical harmonic expansion to represent Betulia's surface displacement and used the "concavity" penalty function to force the model to be quasi-convex-definite. Our goal was to compare this intermediate result (not shown) with the convex-definite lightcurve-based model of Kaasalainen et al. (2004), and indeed our model at this stage was remarkably similar to the two views shown in Fig. 26 of Kaasalainen et al. (Those two views are close to the "$-x$" and "$+y$" principal-axis views of our model in Fig. 4.) Yet even at this stage, despite being heavily penalized, a concavity was developing in Betulia's southern hemisphere in response to our delay-Doppler images. The most obvious signature of this concavity is the "tilde" shape of the echo's leading edge in the first several images on May 29–30 (Fig. 1a): a convex-definite target would instead have produced a concave-downward leading edge.

The final "vertex" stage of the modeling enabled concavities to develop in order to fit the delay-Doppler data. Indeed, the most prominent feature of our final model is the large concavity in Betulia's southern hemisphere, best seen in the "$-y$" view in Fig. 4. The plane-of-sky views in Fig. 1a confirm that

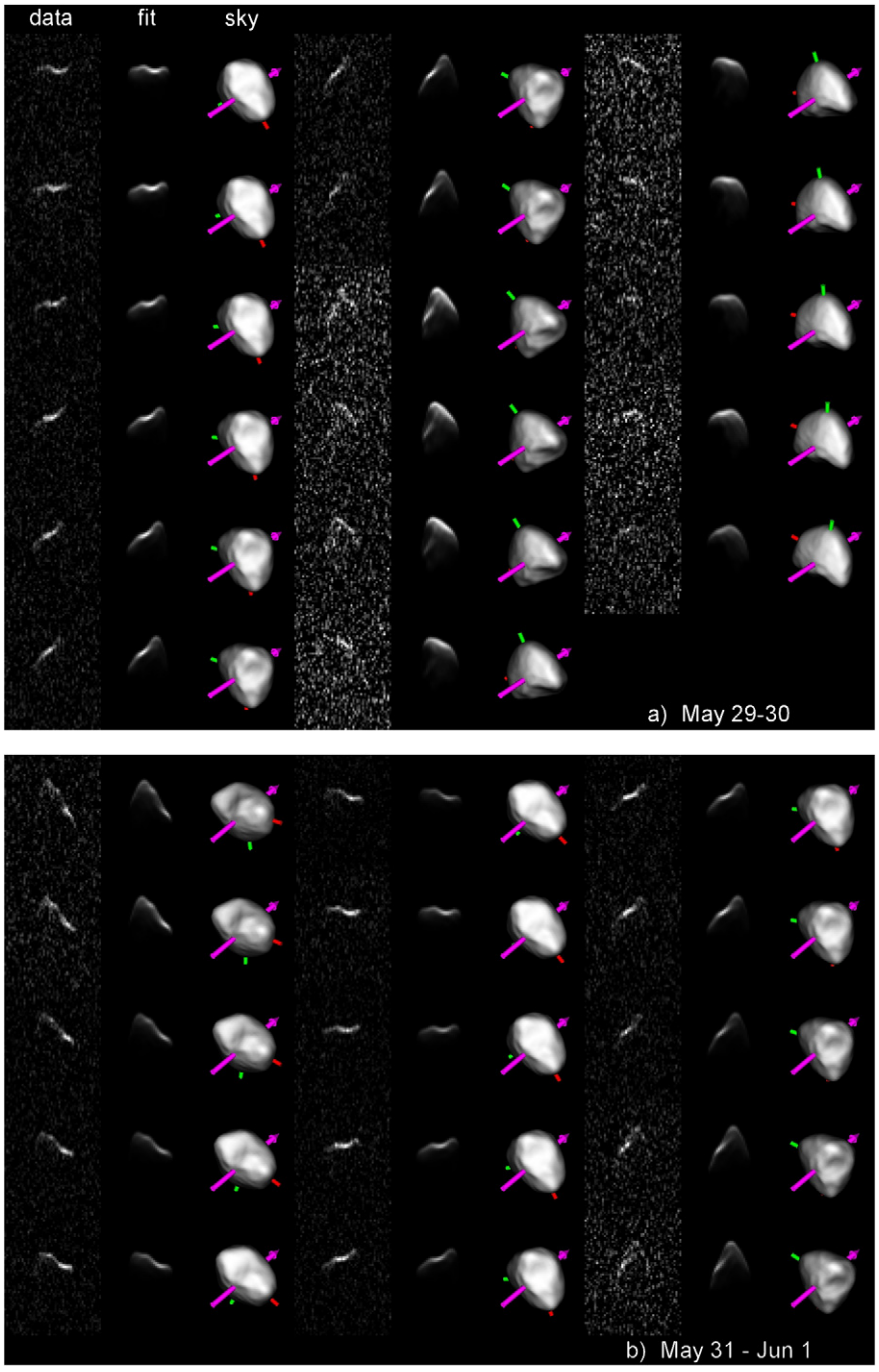

Fig. 1. Betulia delay-Doppler images and model from (a) May 29–30, (b) May 31–Jun. 1, and (c) Jun. 2–3. Each OC image used as input for shape modeling is displayed, with the corresponding synthetic image from the model fit shown to its right, and the corresponding plane-of-sky (POS) rendering of the shape model shown to the right of the synthetic image. In the actual and synthetic delay-Doppler images, Earth is toward the top and positive Doppler is to the right. Each pixel is 0.954 Hz × 1.0 μs, corresponding to 0.28 km × 0.15 km at our mean subradar latitude of −41°; each image spans 47.7 Hz × 60.0 μs, corresponding to 14.0 km × 9.0 km. In the POS frames, north is up and east is to the left. Each POS frame is 9.0 km on a side, and each pixel is 0.09 km on a side. The sidereal spin vector is denoted by a magenta arrow, and the positive ends of the long and intermediate principal axes are denoted by red and green shafts, respectively. POS renderings use the best-fit radar scattering law, with angular exponent $n = 3$ (see Table 2); note the pronounced limb darkening. In each panel time increases from top to bottom and then from left to right.

the tilde-shaped leading edge results from looking directly into this concavity. Additionally, we see in the first few images on May 31–Jun 1 (Fig. 1b) that when this concavity is at the target's limb and approaching us, we get a strong glint in the lower right portion of the image: sections of the concavity's wall that lie well behind the subradar point are directly facing the radar.

We were fortunate to obtain one of our CW spectra just before the first delay-Doppler image on May 29–30, so that we can investigate the echo from the concavity in both OC and

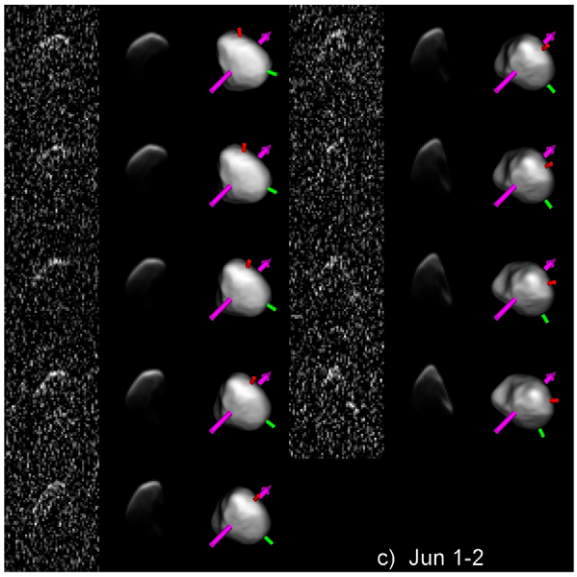

Fig. 1. (*continued*)

SC polarizations. All four single-date dual-polarization CW spectra are shown in Fig. 5. The spectrum from May 29–30 clearly shows a strong OC spike at positive Doppler with no corresponding SC spike; this is a sign of specular scattering from large surface elements that are smooth at decimeter scales. A weaker glint was seen on May 31–Jun. 1, when the same section of the concavity's wall was approaching us but was viewed at a more oblique angle; other glints on the first and fourth runs on May 28–29 (see the two OC spectra in Fig. 2) were produced when the facing wall was receding from us. Perhaps the walls of this concavity have a reduced density of surface rocks, analogous to the reduced density of boulders on the walls of 433 Eros' large craters (Thomas et al., 2002).

Our viewing geometry, with subradar latitude of roughly −40°, was ideal for detecting this southern concavity. It follows that the relative topographical blandness of our model's northern hemisphere might in part be an artifact of this viewing geometry. (Much of this hemisphere is shaded yellow in Fig. 4, indicating regions that received no radar coverage or else coverage at large scattering angles.) However, the Kaasalainen et al. convex-definite model places strong constraints on convex topography, and reveals no large northern planar regions that might represent large concavities in the actual asteroid.

Our model lightcurves fit the optical data fairly well overall; in particular, we are able to reproduce the tertiary lightcurve peak (e.g., 1989 Jun. 3 and 5 in Fig. 3). Residuals are generally only hundredths of magnitudes, with the exceptions of 1976 May 31 and Jun. 1. The fits for 1989 May 25 and Jun. 5 work as well or almost as well as the fits for those two dates displayed in Fig. 27 of Kaasalainen et al., although direct comparison is somewhat difficult since they work in intensity space while we work in magnitude space. Our model also provides a good fit to the 2002 Jun. 2 R-band lightcurve presented in Fig. 6 of Harris et al. (2005), even though we did not use this recent lightcurve as input for shape modeling.

4.2. Size

If lightcurves constrained the overall shape (3-D convex hull) of our model and delay-Doppler images enabled us to "dent" that convex model with concavities, CW spectra were our best guide to the model's overall size. Of course delay-Doppler images also provided information here; but since our Betulia images were weak compared to images of some other NEA targets that we have modeled, spectra were the best mode for measuring echo power near the target limbs. The Doppler bandwidth in turn is directly proportional to the projected distance (breadth) between the limbs.

Our estimate of Betulia's size (see Table 2) is consistent with the radar-based diameter constraint (lower limit) of Pettengill et al. (1979), is smaller than the polarimetric and radiometric diameter estimates of Tedesco et al. (1978) and Lebofsky et al. (1978), and is somewhat larger than either estimate of Harris et al. (2005). Looking at the eight spectral fits in Fig. 2, we see that while we can imagine adjusting the bandwidth of any one of them by 10–20%, it would be hard to obtain a satisfactory overall fit if we shrunk *all* of the bandwidths by 15% to match the effective diameter that Harris et al. obtained from their thermophysical model. We will revisit this issue in Section 7.

4.3. Spin vector

Allowing the model's spin vector—rotation period, pole direction, or both—to vary inevitably resulted in slightly poorer fits than fixing the spin vector at the Kaasalainen et al. (2004) value. As a result, our model uses the Kaasalainen et al. spin vector.

4.4. Disk-integrated properties

Table 3 lists the disk-integrated properties of our model: OC cross section σ_{OC}, OC albedo $\hat{\sigma}_{OC}$ (OC cross section divided by projected area), and circular polarization ratio $\mu_C \equiv \sigma_{SC}/\sigma_{OC}$. The OC albedo of 0.13 ± 0.04 is typical of C-class main-belt targets (Magri et al., 1999; Magri et al., 2006). It implies a near-surface bulk density less than 2.4 g cm^{-3}, an upper limit that is consistent with C-class taxonomy (for lunar-like 50% regolith porosity) but is not very restrictive.

The circular polarization ratio of 0.20 ± 0.03 is fairly low: The mean and median values for 48 radar-observed NEAs are 0.36 and 0.28, respectively, and only eight of the 48 have ratios of 0.20 or lower. (See http://echo.jpl.nasa.gov/~lance/asteroid_radar_properties/nea.sc_oc.html for an updated listing ranked by μ_C.) This low ratio indicates that there is some but not much decimeter-scale structure within a meter or so of the surface. As discussed earlier, the large southern concavity produces a largely specular OC echo—note the low μ_C value in Table 3 on May 29–30 when we were looking directly into the concavity. Hence Betulia is perhaps characterized by heterogeneous radar scattering. Such heterogeneity would represent a limitation of our model, which assumes a simple homogeneous radar scattering law. (Indeed, the OC-only CW spike on May 29–30 is poorly fit by the model—see Fig. 2.) We would want to have

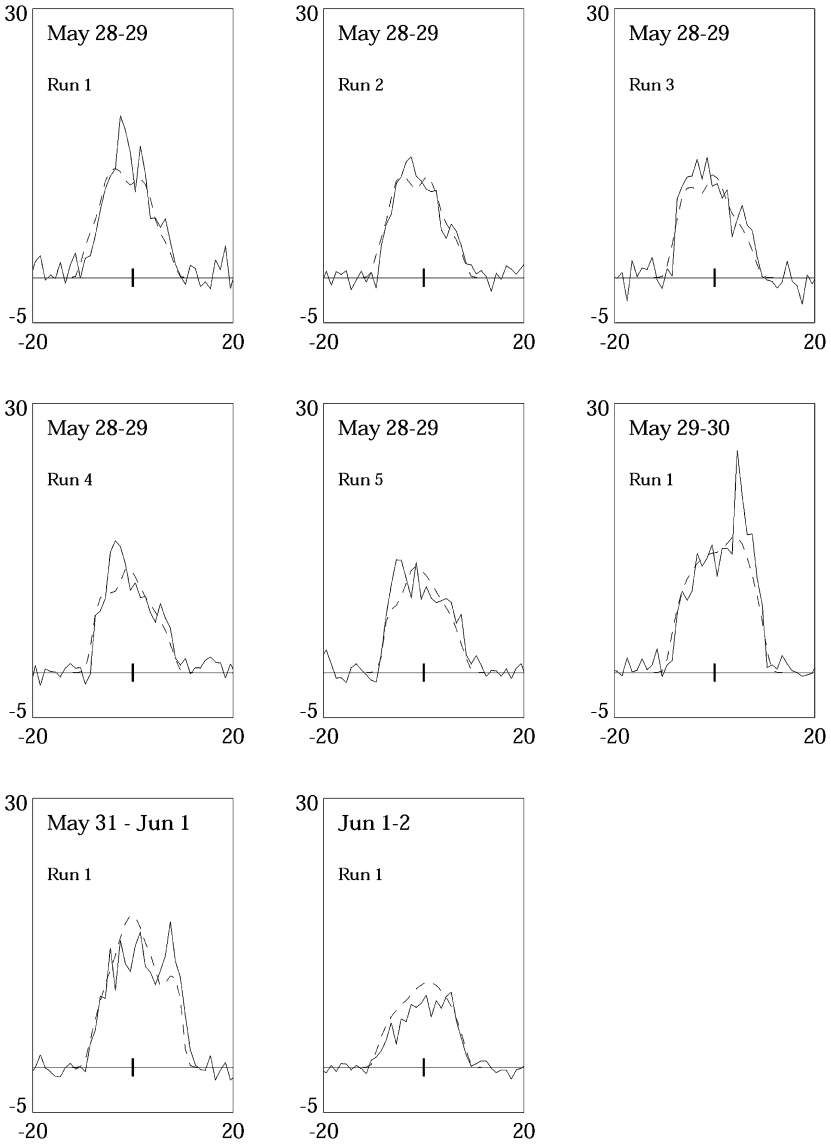

Fig. 2. Betulia CW spectra and model. Echo power, in units of standard deviations of the noise, is plotted versus Doppler frequency (Hz) relative to that of hypothetical echoes from the target's center of mass. Each of the eight OC spectra is displayed as a solid line, with the corresponding synthetic spectrum from the model fit superimposed as a dashed line. The vertical bar at the origin indicates ±1 standard deviation of the noise. Each label gives the observation date and the run number. All spectra are displayed at the raw frequency resolution of 1.0 Hz.

radar data covering a wider range of subradar latitudes before considering a more complex scattering law.

We wish to check for consistency with the CW-based σ_{OC} and μ_C estimates of Pettengill et al. (1979) and Ostro et al. (1991b). The unweighted mean of the seven σ_{OC} estimates in Table 3 is 3.2 km^2; individual values range from 2.5 to 4.5 km^2, a strong rotational variation that is successfully reproduced by our shape model (see Fig. 6). Pettengill et al. found that $\sigma_{OC} = 2.2 \pm 0.8$ km^2. Ostro et al. reported $\sigma_{OC} = 3.9$ km^2 and $\mu_C = 0.16 \pm 0.01$ based on Arecibo data, and $\sigma_{OC} = 4.2$ km^2 and $\mu_C = 0.18 \pm 0.03$ based on Goldstone 3.5-cm data; standard errors on the cross section estimates are about ± 1.0 km^2 (25%) due to systematic calibration uncertainties. Our model predicts a mean cross section of 2.6 km^2 for the 1976 experiment and 3.1 and 3.5 km^2 for the 1989 Arecibo and Goldstone experiments. Given the observational uncertainties, and given the strong rotational variation we find for both σ_{OC} and μ_C, our results are roughly consistent with these earlier studies.

As was mentioned in the introduction, Betulia's high orbital inclination has led to speculation that this object is an extinct comet nucleus. Harmon et al. (2004) show that for five radar-detected comet nuclei, the total radar albedo ($\hat{\sigma}_{OC} + \hat{\sigma}_{SC}$) is no greater than 0.10, averaging about 0.05. Hence Betulia, whose total radar albedo is 0.15 ± 0.04, is unlikely to be an extinct comet.

5. Radar astrometry and orbit refinement

Table 4 presents radar astrometry referred to center-of-mass delay-Doppler locations obtained from the physical modeling, in addition to astrometry from previous radar experiments. For the six 2002 measurements that were obtained via shape mod-

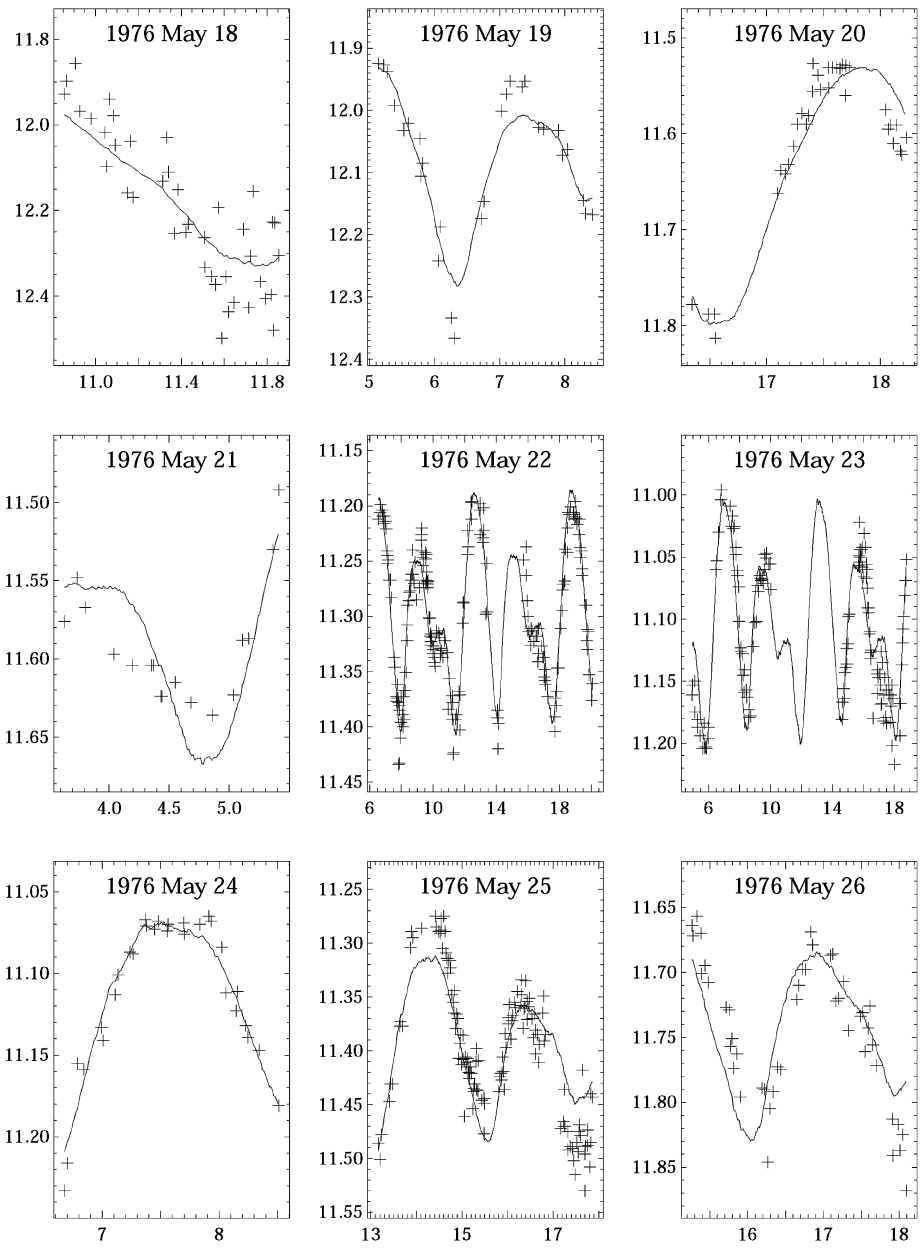

Fig. 3. Betulia lightcurves and model. Units on the x-axis are UT hours on the indicated date. Units on the y-axis are magnitudes; in many cases the magnitudes are absolute, but all lightcurves were treated as relative photometry for shape modeling purposes. Data points for each lightcurve are displayed as crosses and the corresponding synthetic lightcurve is displayed as a solid curve. The two lightcurves for 1989 May 27 were taken in the v and x bands of the eight-color photometric system; see Fig. 45c of Wisniewski et al. (1997).

eling, we set the uncertainties approximately equal to the delay resolution (baud length) and Doppler resolution of the images used in the modeling process.

Table 5 shows orbital elements estimated from the available radar and optical astrometry. Close approaches to planets and large asteroids are listed in Table 6. Our usual criterion for determining the time-span over which close planetary approaches can be predicted is that the 3-sigma uncertainty ("TCA3Sg" in Table 6) in the time of closest approach less than 0.1 AU is less than 10 days and the difference in 3-sigma minimum and maximum approach distance is less than 0.1 AU. Betulia is unusual in that its high-inclination orbit causes it to spend most of its time away from the ecliptic plane, so that it has relatively few close planetary encounters; those that it does have tend to occur at high relative velocities, and are therefore of short duration. As a result, growth in orbital element uncertainties is not a limiting factor for encounter predictability for thousands of years in either direction.

(It follows from this that the reduction in orbit uncertainty provided by our new radar astrometry has not significantly improved our ability to predict close approaches. To check this, we compared close-approach times for orbit solutions obtained with and without the new data for encounters during the timespan A.D. 132–2539, and found that the differences were only on the order of 0.01 day even at the extremes of this range.)

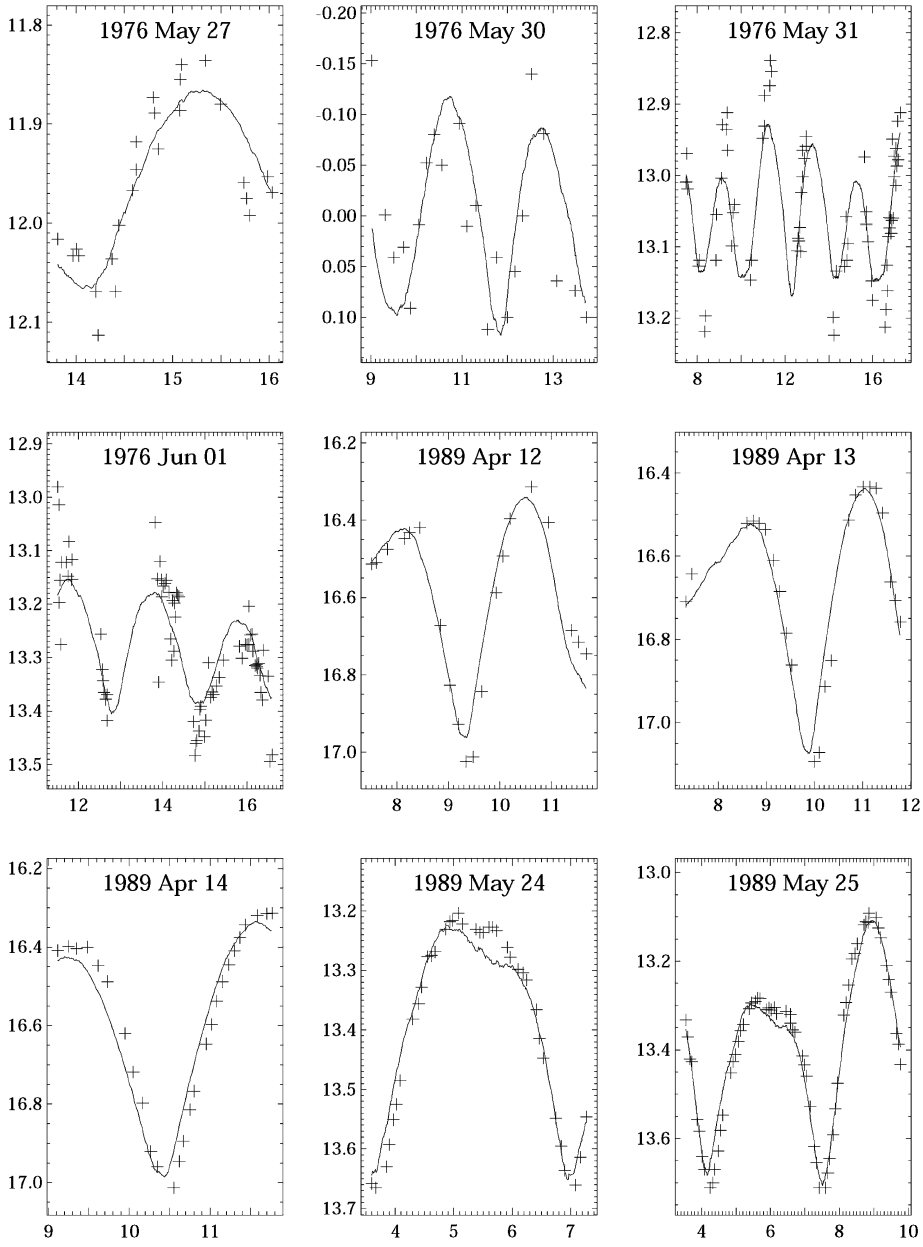

Fig. 3. (*continued*)

Instead the timespan covered by Table 6 is limited by close-approach *distance* uncertainty: the range in possible close-approach distances (the difference between "Max. dist." and "Min. dist." in the table) is greater than 0.1 AU for a 2038 B.C. encounter with Earth, so the table begins at the next Earth encounter in 2025 B.C. This same criterion yields a future Earth encounter prediction limit of A.D. 6395.

6. Gravitational environment

6.1. Dynamical environment parameters

Given the detailed polyhedral shape of Betulia we can compute a variety of quantities directly associated with it. For all our discussions we assume a body-fixed coordinate frame with origin at the body center of mass and aligned with the principal axes of inertia of the asteroid (all computed assuming a uniform density throughout). In light of results from the NEAR mission (Yeomans et al., 2000), this assumption seems reasonable.

It is possible to compute the higher-order mass distributions of the body, which include the inertia moments and the gravitational coefficients up to an arbitrarily high order, using the methodology outlined in Werner (1997). Carrying out these computations we find the moments of inertia:

$$\frac{I_x}{M} = 2.58 \text{ km}^2, \qquad \frac{I_y}{M} = 3.08 \text{ km}^2, \qquad \frac{I_z}{M} = 3.90 \text{ km}^2, \quad (1)$$

where we only quote the moments of inertia divided by the body's total mass M, which is obviously unknown. From the moments of inertia we can solve for the ellipsoid with the same

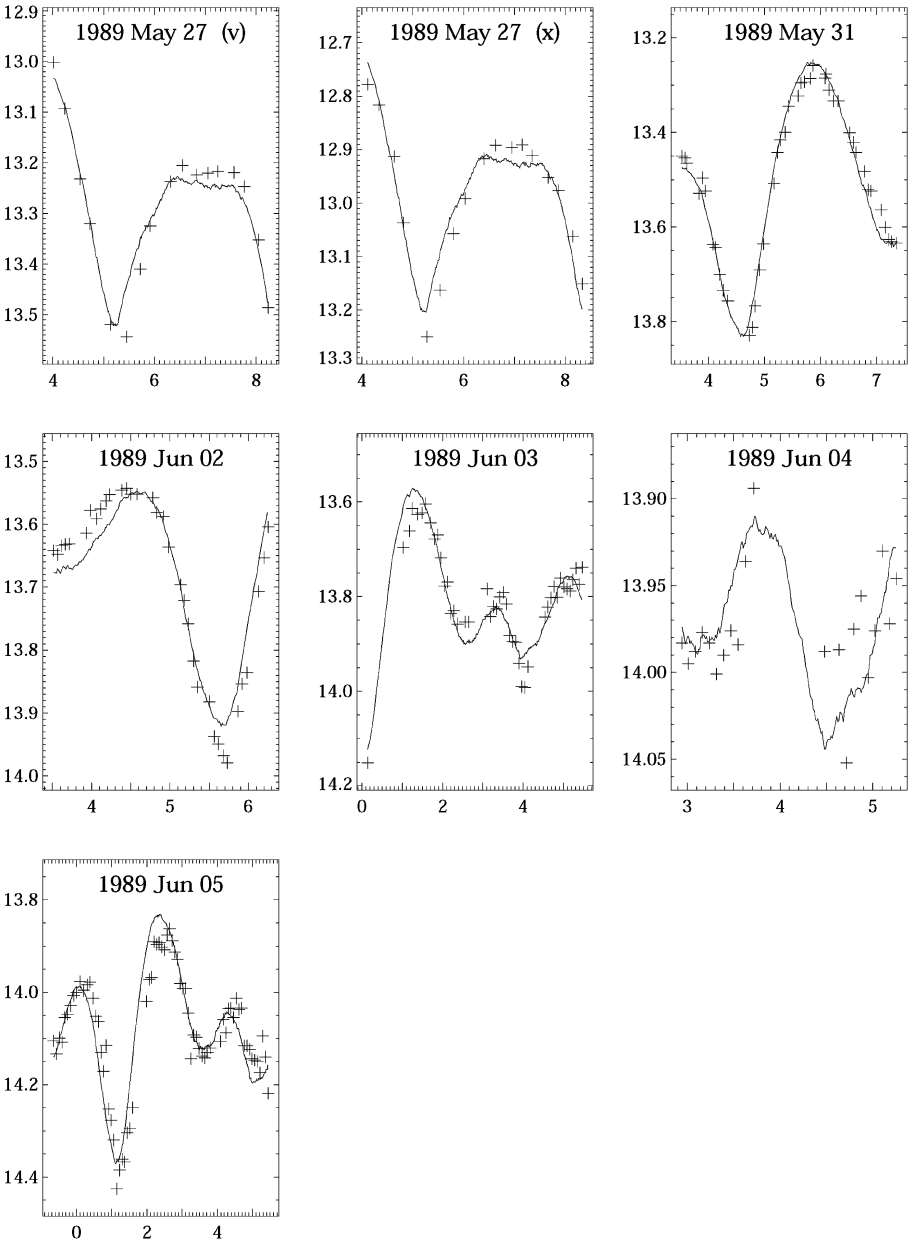

Fig. 3. (*continued*)

moments of inertia, and we find a body with semi-major axes of $3.32 \times 2.92 \times 2.10$ km.

Directly related to moments of inertia are the second degree and order gravity coefficients (e.g., Hu and Scheeres, 2004). These can be directly computed to be

$$C_{20}R_s^2 = -1.072 \text{ km}^2, \qquad C_{22}R_s^2 = 0.125 \text{ km}^2, \tag{2}$$

where R_s is the arbitrary reference radius; these coefficients have not been normalized. A measure of the asteroid's shape and gravity is defined in Hu and Scheeres as

$$\sigma = \frac{I_y - I_x}{I_z - I_x}. \tag{3}$$

For Betulia this value is $\sigma = 0.376$. A body with $\sigma = 1$ has a prolate inertia matrix while one with $\sigma = 0$ has an oblate matrix, thus we see that Betulia has an intermediate index. The gravity field of Betulia has been computed, under the constant density assumption, up to a high degree and order. Appendix C gives the 4th degree and order gravity field in terms of normalized gravity coefficients.

A peculiar feature of Betulia is its triangular shape along its equator. This gives rise to some unique dynamical properties that are intimately related to its gravity field. Due to its shape the 3rd degree and order gravity field coefficients of Betulia are, on average, much larger than for most typical asteroids. The global properties of a gravity field can be estimated by computing the root-mean-square magnitude, σ_n, of the normalized gravity coefficients of each degree,

$$\sigma_n = \sqrt{\frac{1}{2n+1}\sum_{m=0}^{n}\left(\bar{C}_{nm}^2 + \bar{S}_{nm}^2\right)}, \tag{4}$$

Table 2
Properties of the model[a]

Extents along principal axes (km)		x	$6.59 \pm 10\%$
		y	$5.85 \pm 10\%$
		z	$4.19 \pm 10\%$
Extent ratios		x/y	$1.13 \pm 10\%$
		y/z	$1.40 \pm 15\%$
Area (km^2)			$97.2 \pm 20\%$
Volume (km^3)			$82.0 \pm 30\%$
Equivalent diameter of a sphere with the model's volume (km)			$5.39 \pm 10\%$
Ratios of the principal moments of inertia of a uniform-density asteroid with the model's shape		I_Z/I_X	$1.51 \pm 20\%$
		I_Z/I_Y	$1.27 \pm 20\%$
Dimensions of the dynamically equivalent equal-volume ellipsoid (DEEVE, the homogeneous ellipsoid having the same moment-of-inertia ratios and volume as the model) (km)		x	$6.55 \pm 10\%$
		y	$5.77 \pm 10\%$
		z	$4.14 \pm 10\%$
Epoch when the positive side of the longest (x) principal axis is in the plane of the sky while approaching Earth (Julian date)			2452426.65980[b]
Angular radar scattering law exponent n			3.0 ± 1.0
Equivalent spherical OC radar albedo			0.14 ± 0.04
Sidereal period (h)	(from Kaasalainen et al., 2004)		6.13836 ± 0.00001
Pole ecliptic longitude (°)	(from Kaasalainen et al., 2004)		136[c]
Pole ecliptic latitude (°)	(from Kaasalainen et al., 2004)		+22[c]

[a] Listed uncertainties on extents along the principal axes, extent ratios, equivalent diameter, and DEEVE dimensions are conservatively assigned standard errors based on inspecting the results of a large number of modeling runs that started from ellipsoids of various sizes, axis ratios, and angular radar scattering law exponents. Since the model's linear dimensions are uncertain by 10% and its extent ratios by no more than 15%, we assigned 20% uncertainties to area and to ratios of moments of inertia and a 30% uncertainty to the volume. We carried out a multirun grid search using different values of angular radar scattering law exponent n in order to estimate this parameter and its standard error. The standard error on the equivalent spherical OC radar albedo is dominated by the 25% systematic calibration uncertainty on measured OC cross sections. The last three tabulated quantities and their uncertainties are taken directly from Kaasalainen et al. (2004).

[b] This epoch corresponds to UT 2002 Jun. 01 03:50:07. The light from this event reached Earth at JD 2452426.66120 (UT 2002 Jun. 01 03:52:07).

[c] Kaasalainen et al. (2004) state that the error radius on the pole direction is 5–10°.

where the C_{nm} and S_{nm} are the normalized gravity coefficients (Kaula, 2000). Table 7 shows the value of σ_2 and the ratios σ_3/σ_2 and σ_4/σ_2 for several asteroids whose gravity fields have either been measured or estimated from a shape model. If we compare the σ_n for Betulia with other asteroid gravity fields of interest we note the relative importance of its 3rd degree field component as compared to the 2nd and 4th degree contributions. This provides a measure of the importance of the 3rd and 4th degree gravity terms relative to the 2nd degree terms. Other bodies with a strong 3rd degree contribution also have a strong 4th degree contribution. This means that the 3rd degree gravity will play a large role in the orbital evolution close to Betulia.

In order to discuss the dynamical space about the body, we must assume a bulk density. Since the *near-surface* bulk density is less than 2.4 $g\,cm^{-3}$ (see Section 4.4), we assume a density of 2.0 $g\,cm^{-3}$ in the following, realizing that all the subsequent computations would change somewhat given a different density. This choice yields gravitational parameter $\mu \equiv GM = 1.09 \times 10^{-5}\ km^3\,s^{-2}$, where $G = 6.6742 \times 10^{-8}\ cm^3\,g^{-1}\,s^{-2}$.

6.2. Derived dynamical properties for close proximity and surface motions

6.2.1. Close proximity dynamical environment

The simplest parameterization of the close proximity dynamical environment can be made by computing the "resonance radius" of the body, which we define as the distance at which the point mass gravitational attraction of the body equals the centripetal acceleration due to the rotation of the asteroid. This is computed as $r_{res} = (\mu/\omega^2)^{1/3}$, where ω is the rotation rate of Betulia, equal to $2.8433 \times 10^{-4}\ rad\,s^{-1}$. For Betulia this radius is $r_{res} = 5.13$ km, about 1.9 mean radii from the Betulia center of mass. This also corresponds to the ideal Betulia-synchronous orbit radius.

A more precise measure of the close proximity environment is found by precisely computing the orbits synchronous with the rotating body (Scheeres, 1994; Scheeres et al., 1996). For all other uniformly rotating asteroids investigated to date there are only four such orbits, corresponding to true circular orbits about the asteroid with orbit period exactly equal to the rotation period. These orbits appear as equilibrium points in the equations of motion about the asteroid when stated in the body-fixed (i.e., rotating) frame. They generally lie close to the axes of minimum and intermediate moment of inertia.

Due to Betulia's enhanced 3rd degree and order gravity field we find the first exception to this rule. Betulia has a total of six equilibrium points close to its equatorial plane (see Fig. 7). Of these, four are unstable and two are stable. This complex environment is unique among asteroids studied to date, and the existence of stable synchronous orbits implies that there may be ejecta trapped in such orbits at Betulia. We number the equilibrium points starting from the one closest to the x-axis and

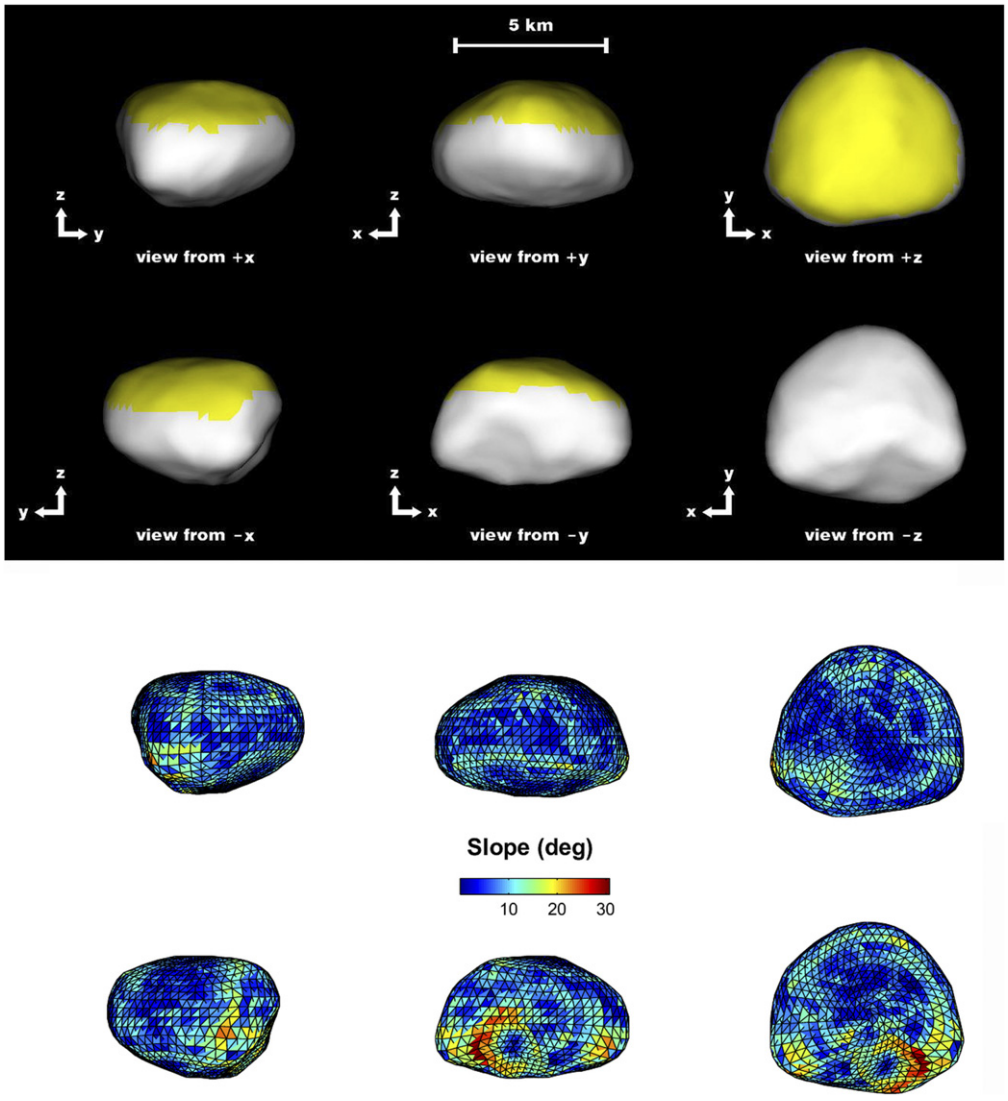

Fig. 4. Views of our Betulia model along its principal-axis directions. The rendering in the upper panel of six views uses a Lambertian backscattering law and has been effectively smoothed as described in Section 3.1.2. Yellow-shaded regions in this panel were never viewed by the radar or else were viewed only at scattering angles greater than 60°. The viewing geometry in the lower panel of six views is identical to that in the upper panel, but these renderings are unsmoothed and are color-coded for gravitational slope in degrees.

increasing counter-clockwise. Their coordinates in a body-fixed frame (x, y, z) are given in Table 8. Points E_1, E_3 and E_5 are hyperbolic unstable (Scheeres et al., 1996) with characteristic times of 1.74, 4.12 and 1.65 h, respectively. Point E_6 is complex unstable with a characteristic time of 3.76 h with an associated period of 8.4 h for the spiral motion. Points E_2 and E_4 are stable, and motion in their vicinity consists of oscillations with three distinct periods, two in-plane and one out-of-plane. For E_2 these periods are 18.0, 7.0 and 5.8 h, while for E_4 they are 19.6, 7.0 and 5.8 h. The longest in-plane periods differ for the two equilibrium points. Based on earlier studies (Hu and Scheeres, 2004) we expect that stable, direct orbits will exist in the equatorial plane at radii above 8 km. Based on that analysis, however, there may be isolated regions of stability between the resonance radius of 5.1 km and 8 km, which is independently consistent with our observed stable equilibrium points E_2 and E_4.

6.2.2. *Surface environment*

Following the methodology outlined in Scheeres et al. (1996), we compute the apparent slope over the surface of the asteroid, the total gravitational plus centripetal accelerations over the body, and the necessary and sufficient speeds for ejecta to escape from the asteroid. As seen in the lower half of Fig. 4, Betulia has a very relaxed surface, with computed slopes ranging up to a maximum of 31°, less than the traditional "angle of repose" for granular material. [During the "vertex" phase of shape modeling we found that lowering the "nonsmooth" penalty weight to permit a rougher surface (see Section 3.3) did not significantly improve our fits, so we instead adopted a fairly smooth model.] The average slope over the body is 8.7°. In terms of distributions of the slopes, 50% of the body has slopes less than 8° and 95% of the body has slopes less than 18°.

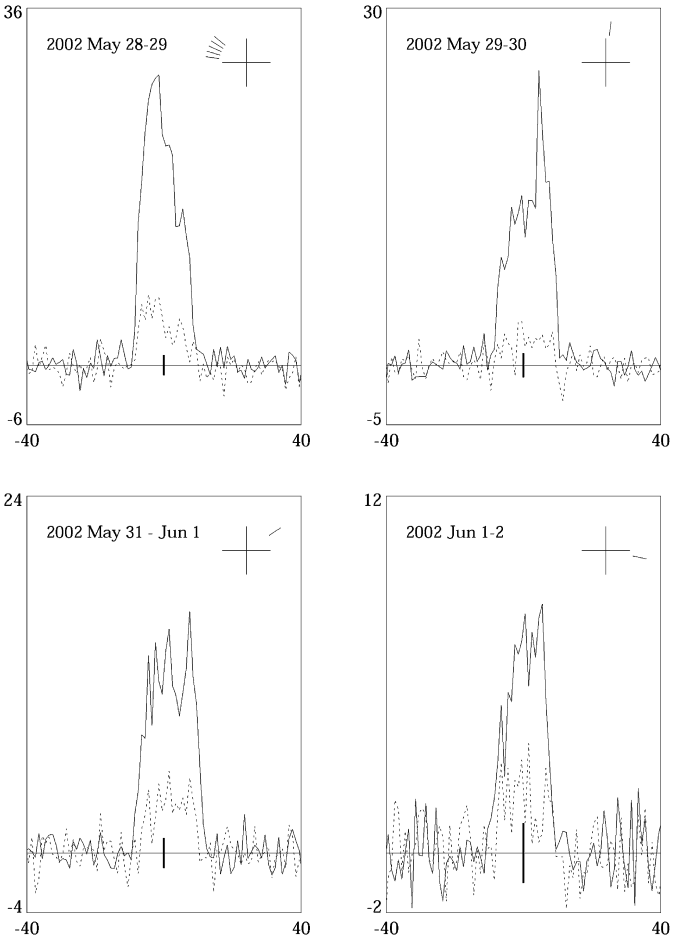

Fig. 5. OC (solid lines) and SC (dashed lines) echo spectra for each of four observing dates on which CW spectra were obtained. The spectrum for 2002 May 28–29 is a weighted sum of five runs; only one run was obtained on each of the other three dates. Echo power, in units of standard deviations of the noise, is plotted versus Doppler frequency (Hz) relative to that of hypothetical echoes from the target's center of mass. (Note the different vertical scales for the four spectra.) The vertical bar at the origin indicates ± 1 standard deviation of the OC noise. Each label gives the UT observing dates. All spectra are displayed at the raw frequency resolution of 1.0 Hz. Rotation phase coverage is depicted in the upper right portion of each plot. Each radial line segment denotes the phase (defined as in Table 1) of a single run; the length of the segment is proportional to the OC noise standard deviation of the corresponding spectrum. Phase increases counterclockwise, with zero phase at the three o'clock position.

The maximum total surface acceleration (combining gravitational and rotational accelerations) is 1.53×10^{-3} m s^{-2} and the minimum is 1.05×10^{-3} m s^{-2}, for a variation of 46% from minimum to maximum. These accelerations can be broken into components normal to the local surface and tangential to the local surface. The accelerations normal to the surface range from 0.99×10^{-3} to 1.53×10^{-3} m s^{-2}. The accelerations tangent to the surface range from ~ 0 to 0.64×10^{-3} m s^{-2}.

The surface environment can also be characterized by the necessary and sufficient surface launch speeds for escape from the asteroid. The necessary launch speeds are the absolute minimum speed a particle must have if it is to escape from the asteroid; that is, any launch speed less than this ensures that the particle will reimpact at some point in the future. Particles with less than the necessary escape speed are confined to lie within the contour in Fig. 7 that passes through the E_5 point and is closer to Betulia. For larger ejecta speeds, these isolating curves open and it becomes possible for ejecta trajectories to escape from Betulia. These necessary speeds range from 1.07 to 1.67 m s^{-1} over the asteroid's surface. Sufficient launch speeds are speeds that ensure that a particle launched in a direction normal to the surface will escape. These speeds range from 2.02 to 3.32 m s^{-1} over the surface. For smaller particles, these speeds will be reduced due to the effect of solar radiation pressure.

7. Discussion

Our Betulia shape model very much resembles a version of the Kaasalainen et al. (2004) convex-definite model to which a large concavity and various small concavities have been added. This general agreement is reassuring but not very surprising: the two studies used essentially the same lightcurve data from the 1976 and 1989 apparitions, and it is lightcurves which constrain the asteroid's 3-D convex hull. (In principle radar data alone can do this, but this requires thorough coverage in subradar latitude and rotation phase; as seen in Table 1, the delay-Doppler images used for shape modeling cover three-quarters of a rotation but only five degrees in latitude.) The agreement between models suggests that convex-definite shape reconstructions—or, in our case, reconstructions that involve a quasi-convex-definite inter-

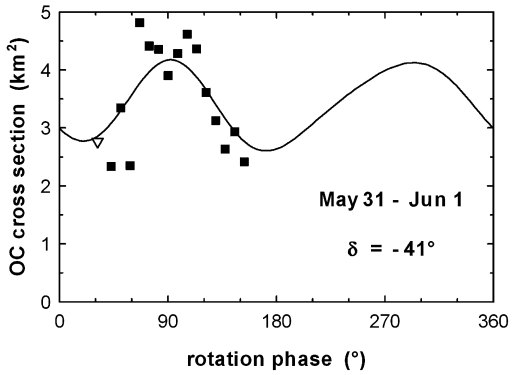

Fig. 6. Observed and predicted OC cross section as a function of rotation phase—the "radar lightcurve"—for 2002 May 31–Jun. 1, when subradar latitude δ was $-41°$. The open triangle and the filled squares are estimates based on CW and delay-Doppler data, respectively; the latter are inherently noisier than the former. The solid line is the predicted lightcurve, which was generated on the assumption of constant $\delta = -41°$. (In fact δ changed by 0.12° between the first and last observations on this date.) Rotation phase is defined as in Table 1. A plot of OC albedo as a function of rotation phase would look approximately the same as the displayed plot (apart from the vertical scale), since the model's projected area is nearly constant with rotation phase (peak-to-peak variation ∼7.5% of the mean projected area).

mediate stage—are indeed robust, as independent studies using independent software packages have reached similar results. Additionally, radar has confirmed that the large planar region in the Kaasalainen et al. model is the site of a large concavity, just as those authors suggested. Lightcurve data are largely insensitive to concavities but can provide broad hints as to their locations.

The main southern concavity has a diameter on the order of Betulia's radius. The only other asteroids known to have such large craters relative to their radii are 4 Vesta (Thomas et al., 1997) and 253 Mathilde (Veverka et al., 1999). Both Betulia and Mathilde are C-class objects, and perhaps the carbonaceous material characteristic of this taxonomic class was conducive to the formation of large craters that did not entirely disrupt these bodies, despite their being much smaller than Vesta. For example, cratering may have occurred through compaction (Housen et al., 1999). But of course it is difficult to generalize when only two such objects are known.

When we consider Betulia's absolute size, we find that our model's maximum diameter is consistent with the radar-based lower limit of Pettengill et al. (1979) but that its effective diameter is somewhat larger than the estimates of Harris et al. (2005). At first this would seem to indicate a conflict: the Pettengill et al. result is consistent with the polarimetric and radiometric size estimates of Tedesco et al. (1978) and Lebofsky et al. (1978), and Harris et al. explicitly state that their results conflict with these earlier estimates. Yet the discrepancy between our model and the Harris et al. thermophysical model is much reduced if we reanalyze two of these earlier datasets.

One of the reviewers, Alan Harris (DLR), points out that applying the Cellino et al. (1999) calibration to the Tedesco et al. polarimetric slope yields a visual albedo of 0.069 ± 0.012, and that this albedo and the Harris et al. (2005) absolute magnitude estimate $H = 15.1 \pm 0.3$ imply a diameter of 4.83 ± 0.78 km, substantially smaller than the 7-km estimate of Tedesco et al. We obtain roughly the same diameter if we use the Tedesco et al. $P_{\min}$ value rather than the polarimetric slope, or if we adopt the Lupishko and Mohamed (1996) calibration rather than that of Cellino et al. Using the brighter 14.8 ± 0.3 H-magnitude estimate of Wisniewski et al. (1997) increases the diameter by 15%, to 5.55 ± 0.90 km.

We also can reanalyze the 1976 radar data: since we now know the viewing geometry for the twenty CW spectra obtained by Pettengill et al. (1979)—for example, the subradar latitude was about +2°—we no longer need to settle for placing a lower limit on Betulia's maximum breadth. Our model predicts zero-crossing bandwidths ranging from 26.4 to 30.1 Hz, with a mean bandwidth of 28.9 ± 2.9 Hz; the uncertainty results from the 10% standard errors on our model's linear dimensions. Pettengill et al. measured a mean zero-crossing bandwidth of 26.5 ± 1.5 Hz, which is within our one-sigma prediction interval. So we can say that our model successfully reproduces the 1976 CW bandwidths, but we also can say that if we increased the effective diameter from 5.4 km to the Lebofsky et al. (1978) value of 7.5 km, the resulting model would badly overestimate those bandwidths.

In short, neither the polarimetric data nor the radar data from the 1976 apparition can still be said to support the 7.5-km diameter estimate of Lebofsky et al. (1978). Hence the entire motivation for that estimate—and for the high-thermal-inertia model that produced it—is removed.

What can we say about the remaining 15% difference between our model's effective diameter and that produced by the Harris et al. (2005) thermophysical model? The difference between 5.39 ± 0.54 and 4.57 ± 0.46 km is only formally significant at about the one-sigma level; nevertheless, we obtain a significantly poorer fit to the radar data if we fit a shape model with the smaller size. This smaller model (not shown) correctly fits the CW bandwidths (to our surprise) but at the expense of getting the cross sections wrong, and its southern concavity is less pronounced so that the quality of the image fits is somewhat degraded. The overall fit is not bad but is not as good as for our adopted model. So we can say that the two models agree much better than did past models but that the remaining difference is still significant.

For completeness we should consider possible problems with our radar-based model. As discussed earlier, it is the Doppler bandwidths of the CW spectra which yield our strongest constraints on the scale of the target. We cannot explain the remaining 15% difference by supposing that we are using the wrong pole direction—a smaller asteroid viewed closer to its equator will yield the same bandwidth—because Harris et al. adopted the Kaasalainen et al. (2004) spin/shape model, and we adopted the same spin vector for our own model. One might instead claim that our radar scattering-law exponent, $n = 3$, is too large (i.e., that our model is too limb-darkened): if echoes from the limbs are weak enough to be lost in the noise, a larger model is needed to match a given bandwidth. But this explanation must also fail, not only because our simulated spectra in

Table 3
Disk-integrated radar properties

Type	Runs	2002 observing date (UT)	Subradar lat., long. (°)	OC SNR	σ_{OC} (km^2)	Proj. area (km^2)	$\hat{\sigma}_{OC}$	μ_C
CW	5	May 28–May 29	−44, 206	83	3.24	25.35	0.128	0.18
CW	1	May 29–May 30	−43, 279	55	4.52	26.61	0.170	0.11
CW	1	May 31–Jun. 1	−41, 328	48	2.76	25.86	0.107	0.24
CW	1	Jun. 1–Jun. 2	−39, 13	24	2.53	24.56	0.103	0.26
							0.127	0.20
Delay-Doppler	17	May 29–May 30	−43, 198	34	2.64	25.45	0.104	–
Delay-Doppler	15	May 31–Jun. 1	−41, 262	45	3.61	25.74	0.140	–
Delay-Doppler	9	Jun. 2–Jun. 3	−38, 4	18	3.34	24.63	0.136	–
							0.127	–

Adopted values and standard errors

$\hat{\sigma}_{OC}$	0.13 ± 0.04
μ_C	0.20 ± 0.03

Notes. For all CW spectra and delay-Doppler images that were strong enough to be used for shape modeling, we list the type of observation, the number of runs, the observing date, the subradar latitude and longitude at mid-receive, the signal-to-noise ratio of the summed OC data, the OC cross section σ_{OC}, the mean projected area, the OC albedo $\hat{\sigma}_{OC}$, and the circular polarization ratio μ_C. Subradar longitude is east longitude measured from the body-fixed $+x$ axis (which is very close to the $+x$ principal axis), and is equal to 360° minus the rotation phase listed in Table 1. We only list μ_C for CW spectra, since delay-Doppler images are inherently noisier than spectra and hence yield far weaker constraints on μ_C. The apparent $\hat{\sigma}_{OC}$ discrepancy between spectra and images for May 29–30 and for May 31–Jun. 1 is partly due to this increased image noise but is largely, according to our shape model, due to strong variation in OC cross section with subradar longitude (see Fig. 6). Average values of $\hat{\sigma}_{OC}$ and μ_C listed for spectra and for images are unweighted means of single-date values. The standard error on our adopted circular polarization ratio reflects date-to-date variations; the standard error on our adopted OC albedo also reflects 25% calibration uncertainty.

Table 4
Radar astrometry[a]

Date (UT)		Data type	Measurement	Residual (sol #72)
Model				
2002 06 03	00:09:00	Delay	248.73123303 s ± 2.0 μs	−1.198 μs
2002 06 03	00:09:00	Doppler	−138,436.315 Hz ± 1.0 Hz	0.136 Hz
2002 06 01	00:57:00	Delay	240.88892798 s ± 2.0 μs	1.851 μs
2002 06 01	00:57:00	Doppler	−80,205.348 Hz ± 1.0 Hz	0.029 Hz
2002 05 30	01:10:00	Delay	237.42002297 s ± 2.0 μs	−0.877 μs
2002 05 30	01:10:00	Doppler	−16,023.930 Hz ± 1.0 Hz	−0.041 Hz
Onsite				
2002 05 28	23:56:00	Delay	237.473411 s ± 10.0 μs	−16.544 μs[b]
Pre-2002				
1989 05 29	00:20:00	Doppler	−72175.0 Hz ± 5.0 Hz	−2.141 Hz
1989 05 28	01:38:00	Delay	185.094484 s ± 12.0 μs	3.161 μs
1989 05 26	01:42:00	Delay	185.537450 s ± 12.0 μs	2.411 μs
1989 05 23	12:00:00	Doppler	501,134. Hz ± 20.0 Hz	2.471 Hz
1976 05 19	05:52:16	Doppler	186012.5 Hz ± 1.0 Hz	−1.549 Hz[c]
1976 05 18	05:56:50	Doppler	225,980.0 Hz ± 1.0 Hz	2.773 Hz[c]

[a] Entries give estimates of the round-trip time delay and Doppler frequency for hypothetical echoes from Betulia's center of mass received at the indicated UT epoch. The first set of six measurements was obtained via shape modeling; we have set the uncertainties approximately equal to the delay and Doppler resolution of the images used in the modeling process. The next listed measurement is a visual estimate made at the start of the 2002 experiment. The last set of six measurements was made during the 1976 and 1989 radar experiments. The 1989 May 23 measurement was made at Goldstone and is referenced to the intersection of the azimuth and elevation axes of the DSS 14 dish. The other twelve measurements were made at Arecibo and are referenced to the main antenna's center of curvature.

[b] This measurement was omitted from orbital solution 72 because of the large residual, because it conflicts with our shape model, and because it was based on a weak image. It is a visual estimate made near the beginning of the 2002 radar experiment in order to update the ephemeris from solution 32 to 34, and represents a delay correction of −200 μs with respect to solution 32.

[c] The two 1976 Doppler residuals suggest that the 1.0-Hz uncertainty estimates are too small. These two Doppler measurements were made by using a spherical model of the target to estimate the midpoints of the two CW spectra; as seen in Fig. 4, Betulia bears only limited resemblance to a sphere, so the uncertainties were probably underestimated. Increasing the assigned uncertainties to 2 or 3 Hz does not significantly change the residuals, indicating that the 1.0-Hz uncertainties are not significantly constraining the orbital solution. However, there is insufficient evidence to conclude that the dynamical model is inadequate.

Fig. 2 show little sign of wide, weak tails, but also because our best-fit models with $n = 1$ and 2 are about the same size (linear dimensions within a few percent, volumes within one percent) as our adopted model.

What, then, will bring the two models into complete accord? The radiometric diameter depends on Betulia's absolute magnitude, and we have seen that the current uncertainty on this magnitude results in a 15% diameter uncertainty. Both models as-

Table 5
Betulia orbital solution (#72)

J2000 heliocentric ecliptic coordinates Epoch 2,453,510.50000 = 2005 May 20.00000				
Osculating element	Value		Post-fit std. dev.	
Eccentricity	0.488002954	±	0.000000025	
Perihelion distance	1.124674339	±	0.000000055 AU	
Time of perihelion	2,453,599.253860 JD	±	0.000013 d	(2005 Aug. 16.75386)
Longitude of ascending node	62.3322519	±	0.0000022°	
Argument of perihelion	159.490079	±	0.000015°	
Inclination	52.095404	±	0.000013°	
Semi-major axis	2.1966422439	±	0.0000000006 AU	
Orbit period	1189.15214571	±	0.00000046 d	(3.25566409161 yr)
Mean anomaly	333.130949010	±	0.000000079°	

Notes. The optical data consisted of 369 usable measurements, with post-fit residual mean and r.m.s. of (0.149, 0.904) arcsec. The normalized r.m.s., obtained by first dividing each measurement by its assigned uncertainty, is 0.751. For the five usable radar delay measurements and seven radar Doppler measurements listed in Table 4, the mean and r.m.s. are (1.07, 1.77) μs and (0.24, 1.71) Hz, and the delay and Doppler normalized r.m.s. values are 0.551 and 1.214, respectively. (See footnote c to Table 4 for a discussion of why the Doppler normalized r.m.s. is somewhat high.) The combined optical-plus-radar normalized r.m.s. is 0.756.

sume homogeneous surface properties, and we have some hints (see Section 4.4) that this is an oversimplification in the case of our radar model. One last item is that, as pointed out by Harris et al. (2005), their thermophysical model "takes no account of surface structure on a spatial scale intermediate between that of craters and that of the whole body"—that is, takes no account of Betulia's large southern concavity, which could "influence shadowing patterns on the surface." We speculate that this concavity significantly influences the surface temperature distribution and hence the disk-integrated IR emission. Repeating the thermophysical analysis with the new radar-based shape model could reveal whether or not this speculation is valid. This represents an excellent opportunity to use a well-observed object to study how a complex shape (a quasi-triangular pole-on silhouette and a large crater) can influence radiometric diameter estimates.

The prospects for further radar study of Betulia are limited, as shown in Table 9. At its next close approach in June 2015, the target will come within 0.35 AU of Earth—nearly 50% further away than in 2002—and will be viewed at subradar latitude −55°, somewhat further south than in 2002. For typical 2006 telescope performance at Arecibo, the expected SNR per date for 2015 CW viewing will peak at 77, so some refinement of the southern hemisphere of our model may be possible. But the 2028 and 2041 apparitions will be at greater distances and hence will be much weaker, so there will be little point in observing at those times. All other close approaches during this century have single-digit SNR per date. In particular, apparitions that would allow us to view the northern hemisphere are not only distant but also reach minimum distance while Betulia is in the southern sky where Arecibo cannot observe it. Hence the current model will likely represent our best estimate of Betulia's shape for some time to come.

Acknowledgments

We thank the Arecibo technical staff for its help with the observations, Mikko Kaasalainen for providing us with archival lightcurve data, and the two reviewers, Alan Harris (DLR) and Mikko Kaasalainen, for helpful comments. C. Magri was partially supported by NSF grant AST-0205975. D.J. Scheeres was partially supported by NASA's Planetary Geology and Geophysics program. J.-L. Margot was partially supported by NASA's Planetary Astronomy program. The Arecibo Observatory is part of the National Astronomy and Ionosphere Center, which is operated by Cornell University under a cooperative agreement with the National Science Foundation. Part of this research was conducted at the Jet Propulsion Laboratory, California Institute of Technology, under contract with the National Aeronautics and Space Administration (NASA). This material is based in part upon work supported by NASA under the Science Mission Directorate Research and Analysis Programs.

Appendix A. Delay-Doppler impulse response function and image calibration

A.1. Impulse response function

As described in Section 3.1.2, for each observing epoch our shape modeling software (SHAPE) generates a plane-of-sky (POS) frame—a simulated diffraction-free optical image of the target—and then determines the contribution of each pixel in this frame to the data obtained at that epoch. In particular, if the observation in question resulted in a delay-Doppler image, SHAPE considers each POS pixel in turn and determines its radar cross section contribution to each pixel in the delay-Doppler image; that is, each POS pixel generally contributes to more than one image pixel. We wish to derive the form of these contributions, the delay-Doppler response function that maps echo power on the sky to cross section in a reduced delay-Doppler image.

Let us be more specific. Suppose we have a POS pixel with area A_{POS}. SHAPE finds the triangular model facet that is projected onto this pixel's center and uses this information to assign a delay d and a scattering angle θ to the entire POS pixel. Doppler frequency f varies continuously across the pixel, since it varies linearly with distance in the plane of the sky perpendicular to the projected rotation axis. The software then maps

Table 6
Betulia close approaches

Date (coordinate time)	Body	CA dist. (AU)	Min. dist. (AU)	Max. dist. (AU)	V_{rel} (km/s)	TCA3Sg (min)
B.C. 2025 Dec. 21.16094	Earth	0.066320	0.045590	0.087555	27.6	1453.7
B.C. 1969 Jun. 26.90882	Venus	0.093067	0.091486	0.094943	31.0	313.09
B.C. 1963 Dec. 20.81244	Earth	0.067125	0.065880	0.068372	27.5	79.20
B.C. 1956 Sep. 09.04350	Venus	0.031427	0.028322	0.034539	28.8	224.72
B.C. 1923 Apr. 21.47408	Venus	0.050049	0.049339	0.050758	32.1	47.36
B.C. 1901 Dec. 15.90302	Earth	0.035467	0.034602	0.036349	29.9	75.67
B.C. 1826 Dec. 13.64580	Earth	0.091225	0.090448	0.092003	31.4	56.33
B.C. 1738 Dec. 18.59925	Earth	0.086714	0.086403	0.087029	27.9	37.29
B.C. 1587 Mar. 01.59140	Venus	0.096266	0.095332	0.097205	26.9	105.02
B.C. 903 Nov. 02.61777	Venus	0.098121	0.097096	0.099154	27.5	127.18
B.C. 874 Aug. 02.81053	Vesta	0.094441	0.094059	0.094826	15.4	48.15
B.C. 749 Jan. 14.74836	Venus	0.073889	0.073127	0.074657	31.0	74.82
B.C. 682 Dec. 05.94811	Vesta	0.056243	0.055930	0.056556	15.3	19.88
B.C. 642 Sep. 02.07489	Venus	0.092343	0.092220	0.092466	27.6	11.70
B.C. 558 Oct. 16.29141	Ceres	0.084880	0.084875	0.084885	15.6	12.89
B.C. 489 Apr. 05.06631	Vesta	0.084707	0.084622	0.084792	15.9	8.52
B.C. 489 Nov. 14.70002	Venus	0.089103	0.088849	0.089358	31.4	17.74
B.C. 348 Feb. 08.85926	Venus	0.084865	0.084539	0.085190	27.7	23.14
A.D. 670 May 10.70755	Earth	0.089186	0.089166	0.089206	29.2	7.96
A.D. 745 May 10.65399	Earth	0.068762	0.068756	0.068769	29.1	4.69
A.D. 820 May 07.49499	Earth	0.079255	0.079164	0.079345	28.7	10.23
A.D. 908 May 12.50263	Earth	0.060499	0.060470	0.060528	29.4	3.13
A.D. 983 May 14.56905	Earth	0.079714	0.079621	0.079807	29.6	7.15
A.D. 1045 May 08.27647	Earth	0.039166	0.039148	0.039184	28.7	1.40
A.D. 1133 May 09.07269	Earth	0.017079	0.017079	0.017079	28.8	0.02
A.D. 1146 May 13.08129	Earth	0.063332	0.063329	0.063335	29.3	0.19
A.D. 1312 May 07.98030	Earth	0.042685	0.042684	0.042685	28.5	0.04
A.D. 1325 May 11.36259	Earth	0.051773	0.051772	0.051773	29.0	0.05
A.D. 1338 May 12.59566	Earth	0.074585	0.074584	0.074586	29.0	0.07
A.D. 1478 May 07.72413	Earth	0.074635	0.074635	0.074636	28.3	0.03
A.D. 1491 May 13.20155	Earth	0.098326	0.098326	0.098327	29.1	0.03
A.D. 1644 May 20.07144	Earth	0.086247	0.086247	0.086247	28.5	0.03
A.D. 3470 Dec. 25.25523	Pallas	0.072523	0.072516	0.072529	20.8	0.56
A.D. 3780 Feb. 05.53399	Pallas	0.086582	0.086580	0.086584	20.5	0.57
A.D. 5494 Jun. 26.64738	Earth	0.079393	0.079392	0.079395	28.6	0.10
A.D. 5660 Jun. 25.53517	Earth	0.058178	0.058175	0.058180	29.0	0.12
A.D. 5673 Jun. 26.75635	Earth	0.047008	0.047006	0.047010	28.9	0.12
A.D. 5686 Jun. 29.87912	Earth	0.082335	0.082332	0.082339	28.5	0.28
A.D. 5852 Jun. 24.64695	Earth	0.085632	0.085625	0.085638	29.7	0.44
A.D. 5865 Jun. 27.71136	Earth	0.029123	0.029121	0.029125	29.1	0.18
A.D. 6063 Jun. 30.38256	Earth	0.020831	0.020828	0.020833	29.1	0.25
A.D. 6076 Jun. 29.25309	Earth	0.020254	0.020252	0.020257	29.3	0.90
A.D. 6089 Jul. 01.12066	Earth	0.046472	0.046378	0.046567	29.1	8.06
A.D. 6229 Jun. 26.23483	Earth	0.097978	0.097968	0.097989	30.2	0.95
A.D. 6242 Jul. 01.17592	Earth	0.049147	0.049144	0.049150	29.4	1.80
A.D. 6395 Jul. 01.77422	Earth	0.076547	0.076530	0.076565	29.6	23.30

Notes. This list includes planetary encounters closer than 0.1 AU. Calendar dates after A.D. 1582 Oct. 15 are reported in the Gregorian calendar; prior to that, dates are reported in the Julian calendar. "CA dist." is the highest probability approach distance of the reference trajectory to the given body. "Min. dist." and "Max. dist." are the 3-sigma distances from the body at the nominal encounter time. "V_{rel}" is the nominal relative velocity. "TCA3sg" is the linearized covariance-mapped 3-sigma uncertainty on the time of closest approach. 1580 Betulia solution #72 was numerically integrated over the interval between 4000 B.C. and A.D. 8000. The list terminates just prior to the Earth encounter for which the time uncertainty ("TCA3sg") exceeds 10 days (14,400 min) or else the distance uncertainty ("Max. dist."–"Min. dist.") exceeds 0.1 AU, whichever occurs first. The span of statistically reliable encounter predictions so-defined is therefore 2025 B.C. to A.D. 6395, based on the solution #72 data-set. Integrations were performed using the DE-408 planetary ephemeris and include relativistic perturbations due to the Sun, planets, and Moon as well as asteroids 1 Ceres, 2 Pallas and 4 Vesta. The limits of predictability for objects having multiple planetary encounters over centuries will normally be affected by additional factors such as radiation pressure, Yarkovsky acceleration, planetary mass uncertainties and asteroid perturbations. Betulia's planetary encounters tend to be fast and distant, mitigating the growth in such perturbative effects, but the factors are not included here since the relevant physical models are imprecisely defined and key parameters are unmeasured.

power from this POS pixel to the various pixels in our delay-Doppler image. Each image pixel has "width" Δf and "height" $\Delta d = b/\chi$, where Δf is frequency resolution, Δd is delay resolution, b is baud length, and χ is the number of image rows per baud. (We typically reduce our images so that χ is the same as the number of samples per baud s, but this need not be the case; for example, we could take data at six samples per baud but then decode only every third delay lag, so that $s = 6$ and

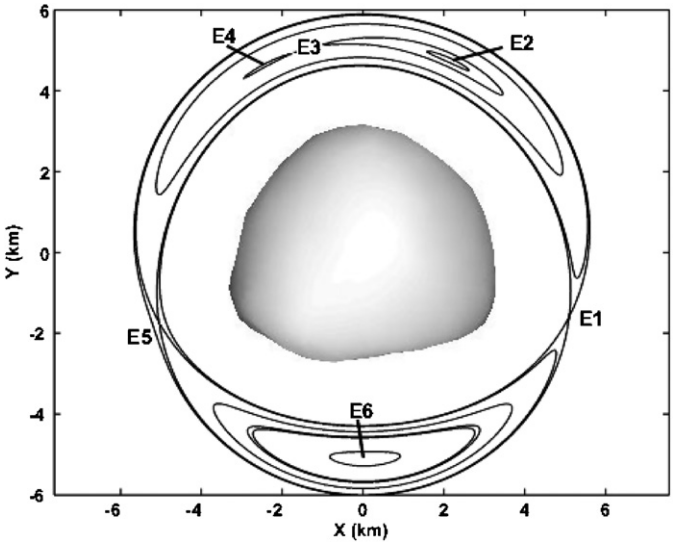

Fig. 7. Zero-velocity curves about Betulia, and locations of the equilibrium points. The axes are in units of kilometers.

Table 7
Gravity power spectra

Asteroid	σ_2	σ_3/σ_2	σ_4/σ_2
1580 Betulia	0.032	0.41	0.18
433 Eros	0.098	0.14	0.23
4179 Toutatis	0.104	0.37	0.82
4769 Castalia	0.085	0.21	0.32
6489 Golevka	0.027	0.48	0.35
25143 Itokawa	0.12	0.33	0.62

Notes. Comparison of gravity power spectra for select asteroids. Quantities σ_2, σ_3, and σ_4 are the r.m.s. magnitudes of the 2nd, 3rd, and 4th degree normalized gravity coefficients [see Eq. (A.4)]. The table provides the value of σ_2 and the ratios σ_3/σ_2 and σ_4/σ_2 for each body. This provides a measure of the importance of the 3rd and 4th degree gravity terms relative to the 2nd degree terms. Data for Eros, Toutatis, Castalia, Golevka, and Itokawa are taken from Miller et al. (2002), Scheeres et al. (1998), Scheeres et al. (1996), Hudson et al. (2000), and Fujiwara et al. (2006), respectively.

Table 8
Equilibrium point locations and stability

Equilibrium point	x (km)	y (km)	z (km)	Stability
E_1	5.101	−1.601	−0.081	Unstable
E_2	2.156	4.742	0.051	Stable
E_3	−1.320	5.056	0.023	Unstable
E_4	−2.500	4.580	−0.004	Stable
E_5	−5.053	−1.717	−0.068	Unstable
E_6	0.065	−5.109	0.062	Unstable

Note. See text for descriptions of each equilibrium point and its stability status.

$\chi = 2$.) We now ask, what does echo power on the sky "within" this POS pixel contribute to the radar cross section σ in an image pixel centered at frequency f_i and delay d_j?

Clearly this contribution will involve the product of the differential scattering law, $d\sigma/dA = \rho \cos^n \theta$, and the area element tangent to the asteroid's surface, $dA = A_{\mathrm{POS}} \sec\theta$. There is also a "code filter" $Y(f)$ to consider. If we take data using a repeating binary phase code of length L, we decode images in the time domain by cross-correlating our voltage samples with a copy of the code, and this shows up in the frequency domain as multiplication by a function whose width is inversely proportional to code repetition time $p = Lb$:

Table 9
Betulia radar opportunities, 2006–2100

Date			RA, Dec. (°)	Subradar lat. (°)	Dist. (AU)	Max. SNR/date
2015	Jun.	03	185, +24	−55	0.352	77
2028	Jun.	08	180, +25	−59	0.478	24
2041	Jun.	14	179, +22	−59	0.584	11

Notes. Radar apparitions between 2006 and 2100 for which the predicted OC signal-to-noise ratio (SNR) per date for CW measurements at Arecibo reaches 10 or greater. Listed quantities are the UT date of maximum SNR per date; the target's right ascension, declination, subradar latitude, and distance from Earth on that date; and the maximum OC SNR per date. We assume typical current Arecibo observing parameters: sensitivity 10 K/Jy, system temperature 25 K, and transmitted power 900 kW. We also assume an OC radar albedo of 0.13 (see Table 3), and we take into account the increase in SNR that results from viewing at high subradar latitude. For comparison, the maximum SNR per date predicted for the 2002 radar experiment was 328.

$$Y(f) = \mathrm{sinc}^2\left(\pi \frac{f}{B}\right), \tag{A.1}$$

where $\mathrm{sinc}\, x \equiv (\sin x)/x$ and unaliased bandwidth $B = 1/p$. In other words, our images are less sensitive as we move away from 0 Hz. Since this variation is slow, we simply evaluate Y using the frequency f at the center of our POS pixel.

It turns out that even a delta-function signal at (f, d) will contribute to more than one image pixel. In the Doppler dimension, the frequency response function $F(f, f_i)$ represents the "ringing" phenomenon which also shows up in CW spectra:

$$F(f, f_i) = \mathrm{sinc}^2\left[\pi\left(\frac{f - f_i}{\Delta f}\right)\right], \tag{A.2}$$

where Δf is the image's frequency resolution. (In deriving this result and those below, we ignore the small quantities $1/L$ and $1/n$, where $n = B/\Delta f$ is the length of the FFT used to produce Doppler spectra at each decoded delay lag.) In practice we must modify this expression in two ways. First, the sinc^2 function has infinite extent, but we do not wish to waste computing time determining very weak contributions from the function's tails. Instead we impose an arbitrary cutoff, zeroing out all contributions beyond three image columns to either side of f. Second, SHAPE deals not with delta functions but with POS pixels, and f varies continuously within each POS pixel. Since F varies rapidly with f, the value of F can change greatly depending on just where within the POS pixel we choose to evaluate it, especially if the pixel is large or the target rotates rapidly. (We cannot make the POS pixels arbitrarily small, since the program runs very slowly if it must repeatedly generate fine-resolution POS frames.) For a rapid rotator we might deal with this problem by evaluating F at four points on a 2×2 grid within the POS pixel and then using the mean of these four function values. Betulia, however, rotates slowly enough that simply evaluating F at the center of each POS pixel was sufficient.

The delay response function $\Delta(d, d_j)$ for one sample per baud is the square of a triangle function that has unit height

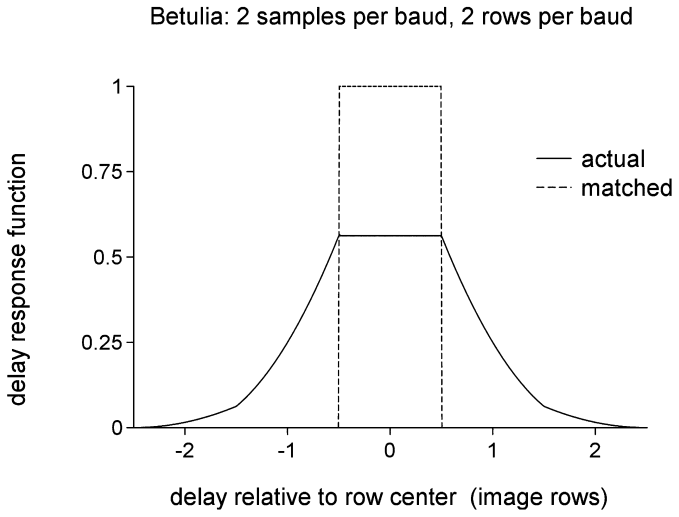

Fig. 8. Response to a delta-function signal in delay for our Betulia images as a function of the difference between the signal delay and the delay at the center of the image row. The dashed line represents a hypothetical (and impossible) matched response, with 100% sensitivity to any signal "within" the row's delay boundaries and 0% sensitivity to any signal "outside" those boundaries. The solid line shows the actual response, a broad (± 2.5 rows $= \pm 1.25$ baud lengths), weak (maximum height 9/16) function of delay. The breadth of the actual response means that within a given Doppler column, the signal in adjacent image rows is significantly correlated. See Appendix A for further discussion.

and half-width b (Harmon, 2002); this results from convolving a baud-length rectangular code element with a matched rectangular filter, then squaring to obtain power. To obtain Δ for s samples per baud we first sum s such triangle functions, with the mth triangle function ($0 \leqslant m \leqslant s-1$) centered at delay $d_j + [m - (s-1)/2](b/s)$. We then divide this sum by s and square it:

$$\Delta(d, d_j) = \left\{ \frac{1}{s} \sum_{m=0}^{s-1} \Lambda\left(\frac{d - d_j}{b} - \frac{m - \frac{s-1}{2}}{s} \right) \right\}^2, \tag{A.3}$$

where triangle function $\Lambda(x) = 1 - |x|$ for $|x| \leqslant 1$ and 0 for $|x| > 1$. (This result is valid to first order in the small quantity fb: we ignore phase differences between different samples within the same baud.) This response function is symmetric in delay, with half-width $[(3 - 1/s)/2]b$; in other words, power on the sky at delay d will contribute to all image rows whose delay d_j is no more than this half-width away from d. It follows that pixel values in adjacent rows are correlated with each other: echo power that is sharply peaked in delay will produce strong pixels in roughly χ adjacent rows in the image. Our Betulia images have $\chi = 2$, thus giving them a "double vision" appearance in the delay dimension.

Putting all of this together, we have the delay-Doppler response function:

$$R(f, d, \theta; f_i, d_j) = \rho \cos^n \theta A_{\mathrm{POS}} \sec\theta \, Y(f) \times \left\{ \frac{F(f, f_i)\Delta(d, d_j)}{\sum_{i'} \sum_{j'} F(f, f_{i'})\Delta(d, d_{j'})} \right\}. \tag{A.4}$$

If we sum this expression over all image columns i and image rows j—that is, if we add up all contributions to the image from incident power at frequency f and delay d—the factor in braces sums to unity and we are left with the factors in front.

SHAPE uses this response function to map power from the plane of the sky to cross section in delay-Doppler space when creating simulated images (see Section 3.1.2). The corresponding impulse response function for simulated CW spectra is the same as Eq. (A.4) but with Y and Δ replaced by unity and no j'-sum in the denominator.

A.2. Image calibration

Let us now consider the various contributions to a particular image pixel centered at (f_i, d_j). Suppose for simplicity that power density $\mathcal{P}$ (power per unit frequency per unit delay) incident on the receiving telescope is uniform in frequency and delay; this assumption will not affect our results. The received power P_R "within" our pixel prior to data reduction is then just $\mathcal{P}\Delta f \Delta d$. However, the signal in the actual reduced image differs from this expression, for two reasons. First, the code filter $Y(f)$ reduces the signal strength. Second, as can be seen in Fig. 8 for our Betulia images, the delay response $\Delta(d, d_j)$ is a weak but broad function, mismatched to the nominal delay resolution; the area under the actual curve is about 1.146 times that under the matched (rectangular) curve. If we integrate the product $YF\Delta$ over all f and d, we find that the signal is approximately equal to $P_R\, Y(f_i) Z$, where "baud filter" Z is given by

$$Z = \left(\frac{11}{20} + \frac{1}{12s^2} + \frac{1}{30s^4} \right) \chi. \tag{A.5}$$

For example, one sample per baud ($s = \chi = 1$) yields $Z = 2/3$ (Harmon, 2002): each pixel has only 2/3 as much signal as if it were 100% sensitive to all incident power within its delay-Doppler boundaries and 0% sensitive to all incident power outside those boundaries. For our Betulia images ($s = \chi = 2$) we instead have $Z = 55/48 \sim 1.146$. When we double s and χ we halve the pixel height (and area), so we would naively expect to halve the signal, but instead the signal only changes by a factor of $[1.146\Delta f(b/2)]/[(2/3)\Delta f b] \sim 0.859$. It remains almost constant because the width of the delay response function Δ increases rather than being halved.

When we take multiple samples per baud, we do not just produce correlated image rows whose pixels have stronger signal than we might have expected; we also reduce the noise, since our time series of voltage amplitudes is effectively smoothed, with consecutive samples correlated with each other rather than independent. This noise is assumed to be thermal noise due to the receiver electronics, to stray scattering in the telescope optics that allows in some thermal radiation from the ground, and to the 3 K microwave background. The total "system temperature" T_{sys} is roughly 20–30 K, and is measured regularly by comparison with a calibrated reference noise source. It is possible to show that the expectation value of the noise power in a single look is equal to the usual $kT_{\mathrm{sys}}\Delta f$ expression (which applies to CW observations) multiplied by "noise factor" η, where

$$\eta = \frac{2s^2 + 1}{3s^2}. \tag{A.6}$$

For Betulia we have $\eta = 3/4$. The r.m.s. noise power fluctuation in an image formed as the mean of N_{looks} independent looks is just the expectation value $\eta k T_{\text{sys}} \Delta f$ divided by the square root of N_{looks}, with N_{looks} equal to integration time τ multiplied by Δf. This r.m.s. fluctuation is usually what we mean by "the noise," since the mean noise power is subtracted out when we normalize our images during data reduction.

We now wish to use the above results to calibrate our image, that is, to determine the cross section that corresponds to one standard deviation of the noise. We define detectability D_{ij} as the ratio of the signal in our pixel to the r.m.s. noise fluctuation; based on the discussion above, we can rearrange this definition to obtain

$$P_R Y(f_i) Z = D_{ij} \frac{\eta k T_{\text{sys}} \Delta f}{\sqrt{\tau \Delta f}}. \tag{A.7}$$

The radar equation tells us that

$$P_R = \frac{P_T G_T G_R \lambda^2 \sigma}{(4\pi)^3 R^4}, \tag{A.8}$$

where P_T is transmitted power, G_T and G_R are the telescope gain when transmitting and receiving, and R is the Earth-target distance. We eliminate P_R from the preceding two equations, solve for σ, and then consider the case where $D_{ij} = 1$:

$$\sigma_{\text{rms}} = \left\{ \frac{(4\pi)^3 R^4 k T_{\text{sys}}}{P_T G_T G_R \lambda^2} \left(\frac{\Delta f}{\tau} \right)^{1/2} \right\} \frac{\eta}{Y(f_i) Z}. \tag{A.9}$$

This is the cross section equivalent of the r.m.s. noise fluctuation. (We have ignored speckle noise due to the echo.) The factor within braces is the expression one would obtain for CW spectra, while the factors that follow are specific to delay-Doppler images. Since the variation in $Y(f_i)$ from column to column is slow, we simply evaluate Y at the COM Doppler frequency rather than computing a different value of σ_{rms} for each column.

In reality, system temperature and gain are not constant during a given Arecibo run: they vary significantly with telescope pointing, due to the telescope's unusual optics. They have been tabulated as a function of telescope pointing using known celestial flux standards (generally quasars). At one-second intervals during the receive half of each run, we found T_{sys} and G_R for the pointing direction at that time, and also G_T for the pointing direction RTT seconds earlier when the signal was transmitted. To obtain the system temperature to be used in the numerator of Eq. (A.9) for this run, we took the square root of the mean of the squares of these individual T_{sys} values (thus adding noise in quadrature); to obtain the product of gains in the denominator, we took the unweighted mean of the individual $G_T G_R$ products.

A.3. Signal-to-noise ratio for summed image subsets

The fact that the noise is effectively smoothed in an image with $s > 1$ also implies that the noise in adjacent rows is correlated. This means that when we sum over an image subset to obtain total cross section, the uncertainty on that sum is not simply the single-pixel noise σ_{rms} multiplied by the square root of the number of pixels N_{pixels}. Here we summarize the results of a lengthy analysis. Two pixels that are in the same Doppler column and are k delay rows apart have correlated noise if $|k| \leqslant k_{\max} \equiv \text{int}[2(s-1)(\chi/s)]$—that is, if the delay difference between the two rows represents no more than $2(s-1)$ sampling intervals. In this case the correlation coefficient r_k is given by

$$r_k = \Big[\big((2s+1-|j|)(2s-|j|)(2s-1-|j|) - 4(s+1-|j|)(s-|j|)(s-1-|j|)\Theta(s-1-|j|)\big) / \big((2s)(2s^2+1)\big) \Big]^2, \tag{A.10}$$

where $j \equiv k(s/\chi)$ is the number of sampling intervals separating the two rows, and step function $\Theta(x) = 1$ for $x \geqslant 0$ and 0 for $x < 0$. If we now sum the noise over a rectangular image subset, and if we consider the simple (and typical) case where the number of rows summed over is much larger than χ, we find that the r.m.s. value for the summed noise is $\sigma_{\text{rms}} \sqrt{N_{\text{pixels}}}$ multiplied by the square root of the sum of r_k from $k = -k_{\max}$ to $k_{\max}$. For Betulia this last factor is about 1.394.

Let us combine all of the results from this Appendix to see what advantage there was in taking two samples per baud for Betulia. Our images have $s = \chi = 2$. We have seen that the signal in each pixel is weaker by a factor of 0.859 than if we had used $s = \chi = 1$, but there are twice as many pixels to sum (twice as many rows) to get the total cross section, giving us a factor of 1.718. The noise in each pixel is only 3/4 what it would have been at one sample per baud, but there are twice as many pixels to sum over (for a factor of $\sqrt{2}$ in the r.m.s. noise), and the noise correlation between adjacent rows provides an additional factor of 1.394; the product of these three values is about 1.479. Hence the signal-to-noise ratio (SNR) is increased by a factor of $1.718/1.479 \sim 1.16$. While taking data at two samples per baud does not improve delay resolution, and does not increase SNR by the $\sqrt{2}$ factor that doubling the number of independent samples would provide, a 16% improvement in SNR is still significant.

There is little advantage to be gained by taking *more* than two samples per baud: one can show that the maximum SNR improvement is about 19% for $s \gg 1$. Since we already have achieved most of this gain for $s = 2$, and since numerous samples per baud means large data files and slow data processing, we seldom take more than two samples per baud in our imaging experiments.

Appendix B. Penalty functions

B.1. Purpose

One purpose of penalty functions is to discourage SHAPE from producing models that fit the data well (low reduced chi-square) but are physically implausible—for example, models that are shaped like sea urchins. Another purpose is to enforce Occam's razor by discouraging complex models (e.g., models whose center of mass is far from the origin, implying nonuniform density) until such time as we have given up on finding a simpler model that fits the data reasonably well.

At the start of each stage (ellipsoid, harmonic, vertex) of each modeling run we specify how many penalty functions will be applied, which particular penalties they will be, and what weight will be used for each penalty. The base value of each penalty function is multiplied by the corresponding penalty weight to give the complete penalty function. Since these penalty functions are added to reduced chi-square to yield the objective function, and since SHAPE tries to minimize the objective function, it follows that a larger penalty weight more strongly discourages the property being penalized.

B.2. Nonsmooth, concavity, and comdev penalties

The "nonsmooth" penalty discourages facet-scale topography, that is, adjacent triangular facets that are not coplanar: its base value is the mean over all model edges of $(1 - \cos\theta)^4$, where θ is the angle between the outward unit normals to the two facets adjoining a given edge. We are generally interested in suppressing topographic structure at scales larger than the facet size, but since such structure necessarily involves some facet-scale structure, this penalty suppresses it.

The "concavity" penalty discourages facet-scale concavities: its base value is the mean over all model edges of the following quantity: $(1 - \cos\theta)^2$ if the edge represents a concavity; 0 otherwise. To determine whether or not a given edge represents a concavity, we look at the two facets adjoining that edge, construct a vector from one end of the edge to the far vertex of facet 1, and take its dot product with the outward unit normal to facet 2. If the dot product is positive, these two facets are tilted relative to each other in the concave sense. We are generally interested in suppressing concavities that are substantially larger than individual facets, but since such concavities necessarily involve some facet-scale concavities, this penalty suppresses them.

The "comdev" penalty tries to keep the model's center of mass (COM) close to the origin of body-fixed coordinates: its base value is the squared length of the COM displacement (in km^2). The COM is actually the center of figure, since it is computed assuming uniform density.

B.3. Inertiadev, inertiadev_uni, nonpa, and nonpa_uni penalties

In order to understand how the next four penalty functions work, we must consider two different ways of determining a model's principal moments of inertia. One method is dynamical: we can choose as free parameters the three principal moments used in Euler's equations to evolve the model's spin state. These three parameters—more precisely, any two ratios of these three parameters—can be constrained by the data for nonprincipal-axis (NPA) rotators but not for principal-axis (PA) rotators. We will refer to these as the "dynamical principal moments": $I_{\mathrm{dyn},x}$, $I_{\mathrm{dyn},y}$, and $I_{\mathrm{dyn},z}$. The other method of obtaining the principal moments is geometric: we obtain the inertia tensor I by integrating over the model's volume (e.g., I_{yz} is the integral over volume of $-yz$ times density) and then diagonalize it. This method works even for PA rotators, but of course SHAPE cannot do the integrals unless it knows something about the model's density—so it assumes *uniform* density. Hence we will refer to I as the "uniform-density inertia tensor" and to the diagonal elements of the diagonalized tensor as the "uniform-density principal moments."

The "inertiadev" penalty is complex in that it does two things to the model simultaneously. The base value of this penalty is $1 - \mathbf{A} \cdot \mathbf{B}$, where vectors **A** and **B** are defined as follows. The three components of **A** are the diagonal elements of I divided by the square root of the sum of squares of all nine elements of I. (That sum is invariant under rotation—such as transformation to principal-axis coordinates.) **A** has unit length if I is diagonal, but is shorter otherwise. To obtain **B**—which is surely a unit vector—we carry out the same procedure with the three dynamical principal moments of inertia, treating them as the diagonal elements of a 3×3 diagonal tensor I_{dyn}. The resulting penalty function is zero if and only if **A** and **B** are identical—that is, if and only if I is diagonal *and* its diagonal elements have the same relative proportions as do the dynamical principal moments. It is positive for any other case.

If I is diagonal then the model's principal axes coincide with the body-fixed coordinate axes—a convenient but physically unimportant feature. Forcing the ratios of the dynamical principal moments to match the ratios of the uniform-density principal moments is more significant, as it means forcing the model to spin like a uniform-density object. That is, it forces the model's density to be uniform. So, to summarize, the "inertiadev" penalty forces the model to have uniform density *and* to have its principal axes aligned with the body-fixed coordinate axes.

This approach is meaningless for PA rotators, since the dynamical principal moments cannot be constrained for such objects. Instead we can use the "inertiadev_uni" penalty, where "uni" stands for "uniform density." This penalty ignores the dynamical principal moments and simply forces the uniform-density inertia tensor I to be diagonal. Put another way, "inertiadev_uni" *assumes* a uniform-density target *and* forces its principal axes to coincide with the three body-fixed coordinate axes. The mathematical function definition is the same as that given above for "inertiadev" except that we replace the dynamical principal moments with the uniform-density principal moments when constructing vector **B**. Applying this penalty is important, as opposed to merely convenient, in that a PA rotator should have its third principal axis coincide with its spin axis (i.e., with the body-fixed z-axis).

The "nonpa" penalty discourages models in which the third dynamical principal moment $I_{\mathrm{dyn},z}$ is smaller than either of the first two dynamical principal moments, since such models would be NPA. To obtain its base value, we compute the fraction by which the largest of the first two dynamical principal moments of inertia exceeds the third dynamical principal moment, then add 0.01 to it, if this results in a negative number, we reset the function to zero. In other words, "nonpa" drives the first two dynamical principal moments to be at least 1% smaller than the third. Again, this is a meaningless approach for PA rotators, since the dynamical principal moments are unconstrained for such objects. In such cases we instead use

Table 10
Betulia normalized gravity field coefficients

Degree l	Order m	Coefficient C_{lm}	Coefficient S_{lm}
0	0	1.0	–
1	0	0.0	–
1	1	0.0	0.0
2	0	−0.0660146	–
2	1	0.0	0.0
2	2	0.0265205	0.0
3	0	0.0036070	–
3	1	−0.0025358	−0.0023070
3	2	−0.0172129	0.0085840
3	3	0.0022822	−0.0280462
4	0	0.0142060	–
4	1	−0.0006590	−0.0005722
4	2	−0.0071511	0.0002485
4	3	0.0029706	0.0041749
4	4	−0.0015610	0.0014316

Notes. Betulia normalized gravity field coefficients through degree and order 4. See text and Appendix C. A gravity field through degree and order 16 is available from the authors.

the "nonpa_uni" penalty, which is identical to "nonpa" except that the uniform-density principal moments are intercompared rather than the dynamical principal moments.

Appendix C. Gravity coefficients

Table 10 lists the Betulia gravity coefficients C_{lm} and S_{lm} through degree $l = 4$. These coefficients are normalized, as defined in Kaula (2000), computed with respect to a normalizing radius $R_s = 2.686$ km. The general form of the gravitational field can be expressed as

$$U = \sum_{l=0}^{\infty} \sum_{m=0}^{l} \left(\frac{R_s}{r}\right)^{l+1} \bar{P}_{lm}(\sin\phi) \times [\bar{C}_{lm} \cos m\lambda + \bar{S}_{lm} \sin m\lambda], \quad \text{(C.1)}$$

where C_{lm} are the normalized Legendre polynomials, ϕ is the particle latitude, and λ is the particle longitude in the body-fixed frame.

References

Brigham, E.O., 1988. The Fast Fourier Transform and Its Applications. Prentice Hall, Upper Saddle River, NJ. pp. 212–217.

Cellino, A., Gil Hutton, R., Tedesco, E.F., Di Martino, M., Brunini, A., 1999. Polarimetric observations of small asteroids: Preliminary results. Icarus 138, 129–140.

Drummond, J.D., Wisniewski, W.Z., 1990. The rotational poles and shapes of 1580 Betulia and 3908 (1980PA) from one apparition. Icarus 83, 349–359.

Fujiwara, A., Kawaguchi, J., Yeomans, D.K., Abe, M., Mukai, T., Okada, T., Saito, J., Yano, H., Yoshikawa, M., Scheeres, D.J., Barnouin-Jha, O., Cheng, A.F., Demura, H., Gaskell, R.W., Hirata, N., Ikeda, H., Kominato, T., Miyamoto, H., Nakamura, A.M., Nakamura, R., Sasaki, S., Uesugi, K., 2006. The rubble-pile Asteroid Itokawa as observed by Hayabusa. Science 312, 1330–1334.

Green Jr., P.E., 1968. Radar measurements of target scattering properties. In: Evans, J.V., Hagfors, T. (Eds.), Radar Astronomy. McGraw–Hill, New York, pp. 1–77.

Harmon, J.K., 2002. Planetary delay-Doppler radar and the long-code method. IEEE Trans. Geosci. Remote Sens. 40, 1904–1916.

Harmon, J.K., Nolan, M.C., Ostro, S.J., Campbell, D.B., 2004. Radar studies of comet nuclei and grain comae. In: Festou, M.C., Keller, H.U., Weaver, H.A. (Eds.), Comets II. Univ. of Arizona Press, Tucson, pp. 265–279.

Harris, A.W., Mueller, M., Delbó, M., Bus, S.J., 2005. The surface properties of small asteroids: Peculiar Betulia—A case study. Icarus 179, 95–108.

Housen, K.R., Holsapple, K.A., Voss, M.E., 1999. Compaction as the origin of the unusual craters on the Asteroid Mathilde. Nature 402, 155–157.

Hu, W., Scheeres, D.J., 2004. Numerical determination of stability regions for orbital motion in uniformly rotating second degree and order gravity fields. Planet. Space Sci. 52, 685–692.

Hudson, R.S., 1993. Three-dimensional reconstruction of asteroids from radar observations. Remote Sens. Rev. 8, 195–203.

Hudson, R.S., Ostro, S.J., Jurgens, R.F., Rosema, K.D., Giorgini, J.D., Winkler, R., Rose, R., Choate, D., Cormier, R.A., Franck, C.R., Frye, R., Howard, D., Kelley, D., Littlefair, R., Slade, M.A., Benner, L.A.M., Thomas, M.L., Mitchell, D.L., Chodas, P.W., Yeomans, D.K., Scheeres, D.J., Palmer, P., Zaitsev, A., Koyama, Y., Nakamura, A., Harris, A.W., Meshkov, M.N., 2000. Radar observations and physical modeling of Asteroid 6489 Golevka. Icarus 148, 37–51.

Kaasalainen, M., Torppa, J., 2001. Optimization methods for asteroid lightcurve inversion I. Shape determination. Icarus 153, 24–36.

Kaasalainen, M., Torppa, J., Muinonen, K., 2001. Optimization methods for asteroid lightcurve inversion. II. The complete inverse problem. Icarus 153, 37–51.

Kaasalainen, M., Pravec, P., Krugly, Y., Šarounová, L., Torppa, J., Virtanen, J., Kaasalainen, S., Erikson, A., Nathues, A., Ďurech, J., Wolf, M., Lagerros, J.S.V., Lindgren, M., Lagerkvist, C.-I., Koff, R., Davies, J., Mann, R., Kušnirák, P., Gaftonyuk, N.M., Shevchenko, V.G., Chiorny, V.G., Belskaya, I.N., 2004. Photometry and models of eight near-Earth asteroids. Icarus 167, 178–196.

Kaula, W.M., 2000. Theory of Satellite Geodesy. Dover Publishing, New York.

Lagerkvist, C.-I., Piironen, J., Erikson, A, 2001. Asteroid Photometric Catalogue, Fifth Update. Uppsala Astron. Obs.

Lebofsky, L.A., Veeder, G.J., Lebofsky, M.J., Matson, D.L., 1978. Visual and radiometric photometry of 1580 Betulia. Icarus 35, 336–343.

Lupishko, D.F., Mohamed, R.A., 1996. A new calibration of the polarimetric albedo scale of asteroids. Icarus 119, 209–213.

Magri, C., Ostro, S.J., Rosema, K.D., Thomas, M.L., Mitchell, D.L., Campbell, D.B., Chandler, J.F., Shapiro, I.I., Giorgini, J.D., Yeomans, D.K., 1999. Mainbelt asteroids: Results of Arecibo and Goldstone radar observations of 37 objects during 1980–1995. Icarus 140, 379–407.

Magri, C., Consolmagno, G.J., Ostro, S.J., Benner, L.A.M., Beeney, B.R., 2001. Radar constraints on asteroid regolith properties using 433 Eros as ground truth. Meteorit. Planet. Sci. 36, 1697–1709.

Magri, C., Nolan, M.C., Ostro, S.J., Giorgini, J.D., 2006. A radar survey of main-belt asteroids: Arecibo observation of 55 objects during 1999–2003. Icarus. In press

Miller, J.K., Konopliv, A.S., Antreasian, P.G., Bordi, J.J., Chesley, S., Helfrich, C.E., Owen, W.M., Wang, T.C., Williams, B.G., Yeomans, D.K., Scheeres, D.J., 2002. Determination of shape, gravity and rotational state of Asteroid 433 Eros. Icarus 155, 3–17.

Ostro, S.J., Campbell, D.B., Chandler, J.F., Hine, A.A., Hudson, R.S., Rosema, K.D., Shapiro, I.I., 1991a. Asteroid 1986 DA: Radar evidence for a metallic composition. Science 252, 1399–1404.

Ostro, S.J., Campbell, D.B., Chandler, J.F., Shapiro, I.I., Hine, A.A., Vélez, R., Jurgens, R.F., Rosema, K.D., Winkler, R., 1991b. Asteroid radar astrometry. Astron. J. 102, 1490–1502.

Ostro, S.J., Hudson, R.S., Benner, L.A.M., Giorgini, J.D., Magri, C., Margot, J.-L., Nolan, M.C., 2002. Asteroid radar astronomy. In: Bottke, W.F., Cellino, A., Paolicchi, R.P., Binzel, P. (Eds.), Asteroids III. Univ. of Arizona Press, Tucson, pp. 151–168.

Pettengill, G.H., Ostro, S.J., Shapiro, I.I., Marsden, B.G., Campbell, D.B., 1979. Radar observations of Asteroid 1580 Betulia. Icarus 40, 350–354.

Press, W.H., Teukolsky, S.A., Vetterling, W.T., Flannery, B.P., 1992. Numerical Recipes in C: The Art of Scientific Computing, second ed. Cambridge Univ. Press, New York.

Scheeres, D.J., 1994. Dynamics about uniformly rotating tri-axial ellipsoids. Applications to asteroids. Icarus 110, 225–238.

Scheeres, D.J., Ostro, S.J., Hudson, R.S., Werner, R.A., 1996. Orbits close to Asteroid 4769 Castalia. Icarus 121, 67–87.

Scheeres, D.J., Ostro, S.J., Hudson, R.S., DeJong, E.M., Suzuki, S., 1998. Dynamics of orbits close to Asteroid 4179 Toutatis. Icarus 132, 53–79.

Shoemaker, E.M., Williams, J.G., Helin, E.F., Wolfe, R.F., 1979. Earth-crossing asteroids: Orbital classes, collision rates with Earth, and origin. In: Gehrels, T. (Ed.), Asteroids. Univ. of Arizona Press, Tucson, pp. 253–282.

Sulzer, M.P., 1986. A radar technique for high range resolution incoherent scatter autocorrelation function measurements utilizing the full average power of klystron radars. Radio Sci. 21, 1033–1040.

Sulzer, M.P., 1989. Recent incoherent scatter techniques. Adv. Space Res. 9, 153–162.

Tedesco, E., Drummond, J., Candy, M., Birch, P., Nikoloff, I., Zellner, B., 1978. 1580 Betulia: An unusual asteroid with an extraordinary lightcurve. Icarus 35, 344–359.

Thomas, P.C., Binzel, R.P., Gaffey, M.J., Storrs, A.D., Wells, E.N., Zellner, B.H., 1997. Impact excavation on Asteroid 4 Vesta: Hubble Space Telescope results. Science 277, 1492–1495.

Thomas, P.C., Joseph, J., Carcich, B., Veverka, J., Clark, B.E., Bell III, J.F., Byrd, A.W., Chomko, R., Robinson, M., Murchie, S., Prockter, L., Cheng, A., Izenberg, N., Malin, M., Chapman, C., McFadden, L.A., Kirk, R., Gaffey, M., Lucey, P.G., 2002. Eros: Shape, topography, and slope processes. Icarus 155, 18–37.

Veverka, J., Thomas, P., Harch, A., Clark, B., Bell III, J.F., Carcich, B., Joseph, J., Murchie, S., Izenberg, N., Chapman, C., Merline, W., Malin, M., McFadden, L., Robinson, M., 1999. NEAR encounter with Asteroid 253 Mathilde: Overview. Icarus 140, 3–16.

Werner, R.A., 1997. Spherical harmonic coefficients for the potential of a constant-density polyhedron. Comput. Geosci. 23, 1071–1077.

Wisniewski, W.Z., Michałowski, T.M., Harris, A.W., McMillan, R.S., 1997. Photometric observations of 125 asteroids. Icarus 126, 395–449.

Yeomans, D.K., Antreasian, P.G., Barriot, J.-P., Chesley, S.R., Dunham, D.W., Farquhar, R.W., Giorgini, J.D., Helfrich, C.L., Konopliv, A.S., McAdams, J.V., Miller, J.K., Owen Jr., W.M., Scheeres, D.J., Thomas, P.C., Veverka, J., Williams, B.G., 2000. Radio science results during the NEAR Shoemaker spacecraft rendezvous with Eros. Science 289, 2085–2088.